THESIS FOR THE DEGREE OF DOCTOR OF PHILOSOPHY IN SOLID AND STRUCTURAL MECHANICS

Predicting crack initiation in highly deformed rail steel

Plasticity modeling, machine-learning-accelerated plasticity simulations, and fatigue criteria

NASRIN TALEBI

Department of Mechanical Engineering
Chalmers University of Technology
Gothenburg, Sweden, 2026

Predicting crack initiation in highly deformed rail steel
Plasticity modeling, machine-learning-accelerated plasticity simulations, and fatigue criteria
NASRIN TALEBI
ISBN 978-91-8103-503-2

Acknowledgements, dedications, and similar personal statements in this thesis reflect the author's own views.

© NASRIN TALEBI, 2026.

Doktorsavhandlingar vid Chalmers tekniska högskola
Ny serie nr 5960
ISSN 0346-718X
https://doi.org/10.63959/chalmers.dt/5960

Department of Mechanical Engineering
Chalmers University of Technology
SE-412 96 Gothenburg
Sweden
Telephone +46 (0)31-772 1000

Cover: An illustration of selected parts of the research presented in this thesis, including machine-learning acceleration of plasticity simulations, prediction of accumulated plasticity, and prediction of fatigue damage initiation in a highly deformed rail.

Printed by Chalmers Digitaltryck,
Gothenburg, Sweden 2026.

To my family.

Predicting crack initiation in highly deformed rail steel–Plasticity modeling, machine-learning-accelerated plasticity simulations, and fatigue criteria

NASRIN TALEBI
Department of Mechanical Engineering
Chalmers University of Technology

Abstract

Rolling Contact Fatigue (RCF) crack initiation, causing major problems for the railway industry, is often associated with large plastic deformations accumulated in the surface layer of rails and wheels. These deformations are known to affect the mechanical and fatigue behavior of the material and to induce anisotropy. Even so, many RCF crack initiation studies do not account for the influence of the deformed near-surface material. Moreover, numerical simulations of the long-term accumulation of plastic deformations under traffic loading are computationally demanding. To address these challenges, the goal of this thesis is to develop methodologies for both more accurate predictions of RCF crack initiation in the highly deformed near-surface rail material and computationally efficient modeling of plasticity.

In the first part of the thesis, a framework is developed for predicting RCF crack initiation in railheads subjected to mixed traffic loading, with a focus on the effects of the highly deformed rail surface layer and profile geometry changes. In particular, an anisotropic material model is calibrated against experiments with railway-like loading at different material states, corresponding to different depths in the railhead. The identified material parameters are then used to consider spatially varying properties in the railhead, governed by an accumulated shear strain distribution reconstructed from measurements in field samples. The framework further incorporates an improved crack initiation criterion that accounts for the accumulated plastic deformations. The findings underline the significant importance of accounting for the deformed near-surface material and rail profile geometry changes when predicting RCF crack initiation.

The second part of the thesis presents two approaches to reducing the computational cost of cyclic plasticity simulations. First, a cycle-domain material model is used to predict peak stress and plastic strain in each loading cycle. Machine Learning (ML) models, Neural Networks (NN) and symbolic regression, are adopted to formulate the per-cycle evolution of plastic strains. Each provides, respectively, high expressiveness and explicit evolution equations. Both ML-based cycle-domain models achieve accurate predictions within and beyond the training regime. As a second approach, an NN-based explicit time integrator is formulated that is capable of taking large strain increments while maintaining accuracy and numerical robustness. The framework is physics-encoded, as it fulfills fundamental plasticity constraints by construction. Material point and finite element simulations demonstrate high accuracy, generalizability, and a considerable reduction in computational time.

Keywords: Railway mechanics, cyclic plasticity, fatigue crack initiation, anisotropy, parameter identification, cycle-domain material modeling, explicit time integration, machine learning, neural network, symbolic regression.

Thesis

This thesis consists of an extended summary and the following appended papers:

[**Paper A**] N. Talebi, J. Ahlström, M. Ekh, K. A. Meyer. "Evaluations and enhancements of fatigue crack initiation criteria for steels subjected to large shear deformations," *International Journal of Fatigue,* vol. 182, p. 108227, 2024.

[**Paper B**] N. Talebi, B. Andersson, M. Ekh, K. A. Meyer. "Influence of a highly deformed surface layer on RCF predictions for rails in service," *Wear,* vol. 578, p. 206173, 2025.

[**Paper C**] N. Talebi, K. A. Meyer, M. Ekh. "Cycle-domain plasticity modeling using neural networks and symbolic regression," *Computers & Structures,* vol. 321, p. 108086, 2026.

[**Paper D**] N. Talebi, M. Ekh, K. A. Meyer. "Machine learning-accelerated time integration of plasticity models," *Computer Methods in Applied Mechanics and Engineering*, vol. 463, p. 119445, 2027.

The appended papers were prepared in collaboration with the co-authors. The author of this thesis was responsible for the major progress of the work, including taking part in the planning of the papers, developing theoretical and computational frameworks, developing the numerical implementations, running the simulations, and writing the papers.

Publication by the author, not included in this thesis, is:

N. Talebi, J. Ahlström, M. Ekh, K. A. Meyer. "Crack initiation criteria for deformed anisotropic R260 rail steel," *CM 2022 - 12th International Conference on Contact Mechanics and Wear of Rail/Wheel Systems, Conference Proceedings,* pp. 857–864, 2022.

Preface

The work presented in this thesis was carried out at the Department of Mechanical Engineering at Chalmers University of Technology within the research project MU41 "Crack initiation in anisotropic wheel/rail material." This project has been part of the ongoing research activities within the Center of Excellence CHARMEC (CHAlmers Railway MEChanics). This study was partially funded within the European Union's Horizon 2020 research and innovation program in the Shift2Rail project In2Track3 under grant agreement number 101012456 and in Europe's Rail project IAM4RAIL under grant agreement number 101101966. Parts of the computations were enabled by resources provided by Chalmers e-Commons at Chalmers.

Acknowledgment

First and foremost, I would like to express my sincere gratitude to my main supervisor, Prof. Magnus Ekh, for patiently mentoring me throughout the past five years and for taking the time to share your invaluable expertise in the field of computational mechanics. Thank you, Magnus, for always making time for your PhD students despite your busy calendar, for your support often at exactly the right moment, for encouraging me to speak Swedish more often, and, more importantly, for caring about my growth, both professionally and personally. I would also like to thank my co-supervisors, Asst. Prof. Knut Andreas Meyer and Prof. Johan Ahlström. Thank you, Knut, for always being open to our discussions, for praising even my smallest achievements, and for your detailed feedback and timely support. Thank you, Johan, for your generous support and for being kind to me. I had the pleasure of working closely with you mainly at the beginning of my PhD project, but your support towards the end of this journey meant a great deal to me.

I would like to extend my appreciation to the CHARMEC group and our research partners for their insightful input and valuable discussions during our workshops and reference group meetings. Special thanks also go to my co-author, Björn Andersson, for the collaboration and a friendly warm-up conversation before our formal meetings.

I am thankful to my colleagues in the Division of Computational Mechanics and Materials Engineering and in the Division of Dynamics for creating an enjoyable work environment. My appreciation also goes to my friends in Sweden and all over the world for making these years more memorable.

I would like to thank my family in my home country for their unconditional love and support throughout these years. Despite the distance between us, you have always been close to my heart, making the challenges of living so far away from home much easier to bear. Last but certainly not least, I would like to express my deepest gratitude to my husband, Kourosh. Thank you for patiently listening to the same presentation over and over again and to my talks about work during your free time! You believed in me when I did not, pushed me to step outside of my comfort zone, and often reminded me to appreciate my achievements. Thank you!

Gothenburg, October 2026,

Nasrin Talebi

Contents

Abstract iii

Thesis v

Preface vii

Acknowledgment ix

I Extended Summary 1

1 Introduction 3
1.1 Background and motivation 3
1.2 Objectives and scope of research 5

2 Rolling contact fatigue crack initiation 7
2.1 The R260 railway rail steel 7
2.2 Fatigue crack initiation in highly deformed rail steel 7
2.3 Fatigue crack initiation criteria 9

3 Material modeling 11
3.1 Generic formulation of small-strain plasticity models 12
3.2 Yield surfaces 12
3.3 Evolution laws for kinematic hardening 13

4 Considered experiments 15
4.1 Predeformation 15
4.2 Multiaxial low cycle fatigue 16
4.3 Uniaxial high cycle fatigue 17

5 Parameter identification using experimental data 19

6 Framework to predict fatigue crack initiation in highly deformed rail steel 21
6.1 Material model calibration 21

6.2 Distribution of accumulated shear strains and anisotropy in railhead cross-section . . . 23
6.3 FE simulations . . . 24
6.3.1 2D axisymmetric simulations of predeformations . . . 24
6.3.2 Wheel over-rolling simulations . . . 25
6.4 RCF damage predictions . . . 27

7 Machine Learning (ML)-based approaches to accelerate plasticity simulations 29
7.1 Motivation and introduction . . . 29
7.2 ML-based cycle-domain plasticity modeling . . . 31
7.2.1 Formulation . . . 32
7.2.2 Numerical performance evaluation . . . 33
7.3 ML-accelerated time integration of small-strain plasticity models 35
7.3.1 Formulation . . . 36
7.3.2 Numerical performance evaluation . . . 37
7.3.3 Application to wheel over-rolling simulations . . . 38

8 Concluding remarks and outlook 41
8.1 Concluding remarks . . . 41
8.2 Outlook . . . 43

Bibliography 45

II Appended Papers A-D 57

Part I

Extended Summary

CHAPTER 1

Introduction

1.1 Background and motivation

Railway transportation is an important mode of transportation due to its high transport capacity, energy efficiency, and contribution to sustainable mobility. At the same time, there is a trend toward increasing operational demands on railway infrastructure, including higher traffic volumes, axle loads, and operating speeds, as well as variations in vehicle characteristics [1]. In Sweden, for instance, the number of train-kilometres travelled on the railway network increased by approximately 34% between 2003 and 2024 [2]. Consequently, the rising demands of railway operation place greater pressure on the durability of wheels and rails and on the ability to predict and manage their degradation.

Repeated loading from wheels rolling over rails causes Rolling Contact Fatigue (RCF), which is recognized as one of the major sources of problems in railway infrastructure [1, 3]. The wheel-rail contact patch is very small, reducing the resistance to rolling of a wheel on a rail, but, in turn, generating very high contact pressures exceeding 1000 MPa [4, 5]. High shear stresses due to traction and cornering forces also act at the wheel-rail contact interface. As a consequence, severe plastic deformations occur in the near-surface material of the contacting bodies [6, 7], as visualized for the rail material in Figure 1.1(a). With repeated wheel passages, the plastic deformations accumulate and induce anisotropic material behavior (directional dependence of the material properties) [8]. These deformations are known to contribute to the initiation of surface RCF cracks at the rail gauge corner, referred to as headchecks [9], as shown in Figure 1.1(b). Wear is another degradation mechanism, involving the removal of material from the contacting surfaces due to slip within the contact patch. Both plastic deformation and wear modify the profile geometries of the wheel and rail.

These changes in profile geometry alter the wheel-rail contact positions and conditions, and thereby influence the subsequent stress distribution, as well as the onset and growth of RCF cracks [10]. If such degradation is not properly managed, it can result in speed restrictions, traffic disruptions, reduced operational reliability, and, in severe cases, rail fracture or derailment. Effective



(a) (b)

Figure 1.1: (a) The deformed surface layer at the gauge corner of a rail [12], (b) gauge corner cracks (Photo: Anders Ekberg).

inspection and maintenance are therefore essential for maintaining a safe and reliable railway system. However, railway maintenance represents a substantial economic cost. For instance, in Sweden, approximately 2.4 billion SEK was spent on track maintenance in 2024 [2]. Another relevant aspect is the environmental impact of railway system maintenance. This was investigated in [11] for a railway crossing in northern Sweden, where CO_2 emissions were found to increase significantly under cold weather conditions. These points highlight the economic and environmental importance of maintenance optimization.

Simulation tools that accurately predict RCF crack initiation–which is a critical stage in the development of rail damage [13]–can aid maintenance planning and can provide a better understanding of the root causes of failures. However, such predictions in the near-surface layer of rails (and wheels) are challenging due to the complex loading conditions and material behavior. The passage of a wheel over a rail generates a complicated multiaxial, non-proportional stress state involving high compressive and shear stresses. In addition, experimental investigations have shown that the highly deformed near-surface material exhibits strong anisotropy in both its mechanical and fatigue behavior [14, 15]. Accordingly, neglecting the influence of this material state when predicting surface RCF crack initiation is a significant simplification. For reliable predictions, therefore, constitutive models capable of describing the complex behavior of the highly deformed near-surface material under such loading conditions, fatigue crack initiation criteria that account for the effects of accumulated plastic deformation, and computationally efficient numerical tools are important.

The need for computational efficiency arises from the large number of loading cycles that should be simulated to obtain more realistic numerical predictions. For instance, traffic on the main railway line in Sweden between Stockholm and Gothenburg is dominated by passenger trains with axle loads ranging from 15 to 19 tonnes, with an annual traffic of approximately $15 \cdot 10^6$ tonnes. This corresponds to about 10^6 wheel passages per year. In addition to the large

number of wheel passages, repeated evaluation of nonlinear constitutive models in Finite Element (FE) simulations of wheel-rail contact situations represents another major source of computational cost. Machine Learning (ML) has found applications across a broad range of disciplines, including constitutive modeling. It has shown promise for improving the accuracy and computational efficiency of constitutive modeling; see, e.g., the review in [16], and accelerating constitutive evaluations at the material point level [17–19].

1.2 Objectives and scope of research

The overall aim of the research in this thesis is to enhance the predictive capability and computational efficiency of numerical tools for simulating the mechanical response and for fatigue crack initiation analysis of railway rails subjected to traffic loading. Particular emphasis is placed on accounting for the heavily deformed near-surface material. To achieve this overall objective, the research is divided into two related parts. The first concerns the influence of severe plastic deformations on RCF crack initiation predictions. The second aims to develop computationally efficient approaches for (cyclic) plasticity simulations, with the ultimate objective of enabling efficient simulations of wheel-rail contact situations to account for the long-term evolution of rail material properties and rail profile geometry under operational loading. The following research objectives are defined in this thesis:

1. Determine a suitable fatigue crack initiation criterion that takes into account the effect of the highly deformed material in the surface layer of rails.

2. Develop a framework to investigate the impact of the highly deformed near-surface material and deformed rail profile geometry on RCF crack initiation predictions in railheads under mixed traffic loading.

3. Develop computationally efficient ML-based approaches for simulating cyclic plasticity, with a focus on reducing the computational cost of resolving material evolution over many loading cycles.

The scope of this thesis is limited to fatigue crack initiation and does not include the subsequent propagation of macroscopic RCF cracks. The material investigated is R260 pearlitic rail steel, but the developed approaches can also be relevant for studying wheels and other materials. The experimental data used to calibrate and validate the material models and fatigue crack initiation criteria were obtained from a previous project in the CHARMEC research group. The influence of accumulated plastic deformation is studied at the continuum scale, with the deformation-induced anisotropy represented through macroscopic constitutive and fatigue models rather than through an explicit description of the pearlitic microstructure.

CHAPTER 2

Rolling contact fatigue crack initiation

2.1 The R260 railway rail steel

The material considered in this thesis is the R260 railway rail steel with Brinell hardness ranging from 260 to 300 and the chemical compositions presented in Table 2.1. This rail steel is typically used in lightly loaded tracks with radii larger than 1000 m, where wear is not the dominant degradation mechanism [20].

This material has a pearlitic microstructure, consisting of hard cementite lamellae (bright contrast) embedded in a softer ferrite matrix (dark gray contrast); see Figure 2.1. In the undeformed material state, in each pearlite colony, the cementite lamellae are relatively aligned compared to those in the neighboring colonies, as shown in Figure 2.1(a). However, Figure 2.1(b) shows the deformed material that has undergone severe plastic deformation, where the cementite lamellae are reoriented and highly aligned.

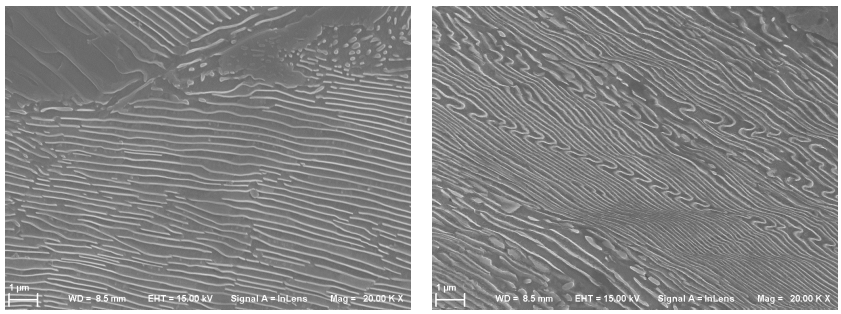
Table 2.1: Chemical composition (in mass percentage) of the R260 rail steel according to EN 13674 [21].

C	Si	Mn	P	S	Cr	Al	V	N	Cu
0.82	0.60	1.25	0.03	0.03	0.15	0.004	0.03	0.01	0.15

2.2 Fatigue crack initiation in highly deformed rail steel

High normal and shear stresses generated during wheel-rail contact cause severe plastic deformations in the near-surface material of rails. The progressive accumulation of plastic deformations aligns the material microstructure, resulting in anisotropic behavior [23]. Laboratory investigations of in-service rails have shown alignment of cementite lamellae in the rolling direction, substantial shear strains, and increased hardness near the rail surface [7, 8, 24].

Several experimental methods have been used in the literature to reproduce the severely deformed surface layer of in-service rails in the laboratory,



(a) The undeformed material state (b) The deformed material state

Figure 2.1: Scanning electron microscope image of the pearlitic microstructure consisting of the cementite lamellae in the ferrite matrix, from [22].

including equal channel angular pressing [14], high-pressure torsion [15, 25], and predeformation [12, 26]. These studies have shown that severe plastic deformation affects fatigue, fracture, and mechanical properties of rail steel. For instance, Leitner et al. [27], by performing high pressure torsion tests on fully pearlitic steel, found reduced fatigue crack resistance along aligned cementite lamellae, promoting crack growth along the elongated microstructure. Further, Gren and Ahlström [28] reported a lower fatigue crack propagation rate in predeformed material than in undeformed material.

The highly deformed near-surface material in rails is known to be the region of interest for the initiation of head checks [9]. These surface-initiated RCF defects are commonly observed as regularly spaced cracks at the gauge corner of the high rail in curves, where lateral traction is increased to provide the forces required for cornering [3, 29, 30].

Wear is another important degradation mechanism in rails that interacts with RCF crack initiation at different length scales. At the wheel–rail contact scale, wear modifies the contacting profiles, thereby changing the contact conditions and resulting contact stresses [31]. Wear can be beneficial when the wheel and rail profiles evolve towards improved conformity, resulting in a larger contact patch and lower contact stresses. Conversely, unfavorable profile evolution may lead to locally increased contact stresses, thereby increasing the risk of both wear and RCF crack initiation [29].

According to the delamination theory of wear [32], cracks growing approximately parallel to the surface in highly shear-deformed material may eventually detach thin layers of material as wear particles from the surface. Building upon this, in [33], it has been proposed that depending on the distribution of accumulated shear strains and contact stresses in the severely deformed near-surface material, wear can counteract the development of microscopic RCF cracks into macroscopic cracks.

For the investigations in **Paper B**, the influence of wear was considered through the rail profile geometry. A worn rail profile measured in [12] was used in multibody dynamics simulations to obtain contact forces and contact

positions, and was subsequently used in the FE simulations of train wheel over-rollings. Thus, the effect of wear-induced profile geometry changes on the wheel-rail contact conditions and RCF damage predictions was implicitly taken into account. During the considered short snapshot in the rail life, corresponding to 348 wheel passages, the interplay between wear and RCF crack initiation was assumed to be negligible.

2.3 Fatigue crack initiation criteria

To assess how severely deformed near-surface material and changes in rail profile geometry influence the risk of RCF crack initiation, a framework for predicting fatigue crack initiation is required. This, in turn, necessitates the use of a crack initiation criterion capable of accounting for material state and the complex loading condition associated with wheel-rail contact.

For prediction of fatigue crack initiation, coupled and uncoupled approaches can generally be employed. In coupled approaches, such as continuum damage mechanics [34], the evolution of fatigue damage is incorporated into the mechanical formulation such that the accumulated damage affects the material response. In contrast, uncoupled approaches assume that fatigue damage does not affect the macroscopic material response before crack initiation. Consequently, the stress and strain histories can first be obtained from the mechanical analysis, and fatigue damage or life can subsequently be predicted in a post-processing step. In this thesis, an uncoupled approach has been adopted. This was motivated by the experimental findings in [26], where it was shown that predeformation did not significantly affect shear and Young's moduli.

Many crack initiation criteria for rolling contact loading conditions have been proposed in the literature; see the reviews by Sadeghi et al. [35] and Ringsberg et al. [36]. Examples include the equivalent plastic strain model proposed by Kapoor [37], the pure energy-density based criterion developed by Golos and Ellyin [38], and approaches that incorporate material microstructure in fatigue damage predictions [33, 39–41]. Some criteria employ a critical plane search approach to identify the highly damaged plane [42–46]. Jiang and Sehitoglu [47] proposed that fatigue damage evolution on a given plane is influenced by normal and shear stress and strain ranges. Since wheel-rail contact loadings produce multiaxial non-proportional stress and strain states, a multiaxial fatigue criterion that also accounts for the varying principal directions of the stress and strain tensors with time is required for accurate crack initiation predictions.

In **Paper A**, it was shown that, due to the protective effect of predeformation (see Section 4.1 for further details regarding the predeformation technique), the mixed criterion [47], combining the Jiang-Sehitoglu (J-S) and Kapoor criterion, does not provide noticeable improvement. Therefore, two modifications to the J-S criterion to improve its predictive capabilities was proposed. In the original J-S criterion [47], a constant threshold for damage accumulation, FP_0, is introduced. However, in **Paper A**, it was shown that the

predictive accuracy can be improved by letting this depend on the accumulated ratcheting strain, ϵ_r, as

$$\widetilde{FP}_0\left(\epsilon_{\mathrm{r}}\right) = FP_\infty - \left[FP_\infty - FP_0\right] \exp\left(\frac{-\epsilon_{\mathrm{r}}}{\kappa}\right) \tag{2.1}$$

The cyclic fatigue damage growth is then computed as

$$\frac{\mathrm{d}D_{\mathrm{f},i}}{\mathrm{d}N} = \left[\frac{\left\langle \max_{\boldsymbol{n}} FP - \widetilde{FP}_0 \right\rangle}{C_0}\right]^m \tag{2.2}$$

where $\langle \bullet \rangle = 1/2(\bullet + |\bullet|)$ is the Macaulay bracket. The fatigue driving force, FP, on a given plane is quantified following [47]

$$FP = \sigma_{\max} \frac{\Delta\epsilon}{2} + J\,\Delta\tau\,\Delta\gamma \tag{2.3}$$

The fatigue parameters, m, C_0, J, FP_∞, κ, and FP_0, were calibrated against the predeformation, high cycle fatigue, and proportional multiaxial low cycle fatigue tests, described in Chapter 4. The proposed modifications were intended to capture the increased resistance to fatigue crack initiation associated with predeformation, motivated by the findings of Gren and Ahlström [28]. Figure 2.2 compares the agreement with the experimental data obtained using the original J-S criterion and the modified criterion, J-S ($\widetilde{FP}_0$). The modified criterion improved the overall agreement, particularly for the cyclic tests, Exps. 5-9.

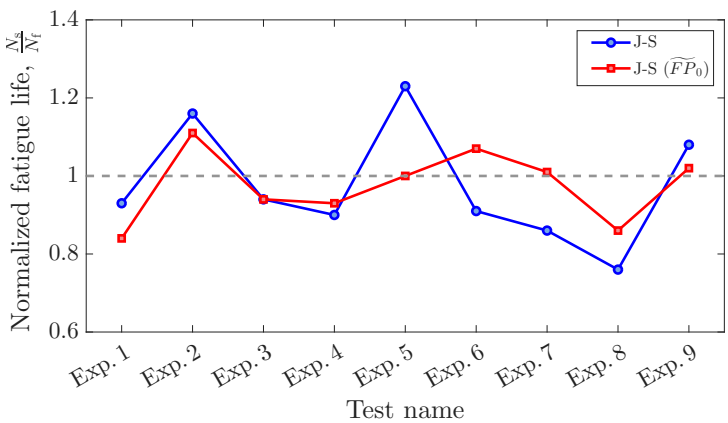


Figure 2.2: Normalized fatigue lives from the original J-S and modified J-S criterion ($\widetilde{FP}_0$). The horizontal line indicates perfect agreement between the simulated and experimental fatigue lives. Exps. 1-4 refer to predeformation tests, and Exps. 5-9 refer to cyclic tests preceded by predeformation; see Chapter 4 for further details regarding the experiments.

CHAPTER 3

Material modeling

Reliable predictions of plasticity-induced fatigue crack initiation require careful modeling of the material's stress and strain histories. As discussed in Chapter 2, severe plastic deformations occur in the near-surface material of railway rails under wheel-rail contact loading [48]. As a consequence of progressive accumulation of the plastic deformations, the material microstructure aligns along the principal deformation direction, leading to anisotropic yielding behavior [49]. Micromechanical models, such as those in [50, 51], are useful for understanding the mechanisms occurring in the material's microstructure. However, their high computational cost when implemented in an FE framework can limit their applicability in wheel-rail contact simulations.

A further modeling choice is the kinematic framework in which the constitutive equations are formulated. Small-strain kinematics provides an appropriate basis for constitutive modeling in many engineering problems. Its use may also be motivated by computational efficiency. This is particularly relevant in wheel-rail rolling contact simulations [52], where a large number of loading cycles may need to be considered. Although large shear strains develop in the near-surface material during long-term cyclic loading, the use of finite-strain kinematics can substantially increase the computational cost. For instance, Meyer et al. [53] simulated individual cycles of wheel–rail contact using an efficient 3D FE formulation with a finite-strain material model. The computational time was approximately 0.7 minutes per cycle (for a rolling length of 30 mm) using 10 cores on a computer cluster. However, considering an annual traffic of 10^6 wheel passages on the passenger train-dominated main railway line between Stockholm and Gothenburg in Sweden, such a simulation would require considerable computational time.

In **Papers A and B**, a finite-strain model formulation was adopted for FE simulations of the predeformation tests, replicating the large shear strains in the surface layer of in-service rails (described in Section 4.1). In **Papers C and D**, as well as for the majority of the simulations in **Paper B**, small-strain plasticity formulations were used, with further details explained in the following.

3.1 Generic formulation of small-strain plasticity models

A generic small-strain, rate-independent plasticity model starts from the Helmholtz's free-energy function, Ψ, expressed in terms of the total strain, $\boldsymbol{\epsilon}$, and the set of N_s state variables, $\mathbb{S} = \{\mathfrak{s}_1,\ \mathfrak{s}_2,\ \cdots,\ \mathfrak{s}_{N_\mathrm{s}}\}$,

$$\Psi = \Psi\left(\boldsymbol{\epsilon}, \mathbb{S}\right) \tag{3.1}$$

The stress, $\boldsymbol{\sigma}$, and the (hardening) variables, $\mathbb{A} = \{\mathfrak{a}_1,\ \mathfrak{a}_2,\ \cdots,\ \mathfrak{a}_{N_\mathrm{a}}\}$, are obtained as

$$\boldsymbol{\sigma}(\boldsymbol{\epsilon}, \mathbb{S}) = \frac{\partial \Psi}{\partial \boldsymbol{\epsilon}}, \quad \mathfrak{a}_i(\boldsymbol{\epsilon}, \mathbb{S}) = -\frac{\partial \Psi}{\partial \mathfrak{s}_i}$$

The elastic domain is then characterized by a yield function, $\Phi\left(\boldsymbol{\sigma}, \mathbb{A}\right)$, where $\Phi < 0$ corresponds to elastic behavior and $\Phi = 0$ defines the plastic domain. By introducing the plastic multiplier, $\dot{\lambda}$, the Karush-Kuhn-Tucker (KKT) loading/unloading conditions are expressed as

$$\Phi \leq 0, \quad \dot{\lambda} \geq 0, \quad \Phi\,\dot{\lambda} = 0 \tag{3.2}$$

The state variables only evolve during plastic loading, which can be described by the generic evolution laws,

$$\dot{\mathfrak{s}}_i = \dot{\lambda}\,\mathfrak{f}_i\left(\boldsymbol{\sigma}(\boldsymbol{\epsilon}, \mathbb{S}),\ \mathbb{A}(\boldsymbol{\epsilon}, \mathbb{S})\right) \tag{3.3}$$

Depending on the experimental loading path or the objective of numerical simulations, the material model may incorporate isotropic hardening, kinematic hardening, or a combination of both, with suitable evolution laws for each state variable, $\mathfrak{s}_i$. For instance, Pack et al. [54] employed only an isotropic Swift-Voce hardening law in the chosen material model to predict the experimentally observed material behavior under monotonic loading. It is, however, well-established that kinematic hardening is essential for accurately capturing the yielding behavior and the associated Bauschinger effect during load reversal in cyclic loading [55]. Nevertheless, kinematic hardening alone may not be sufficient to reproduce all features of cyclic plasticity. For example, in [56], to account for the decay of ratcheting rate in cyclic plasticity simulations when using the Armstrong-Frederick (AF) kinematic hardening law [57], the use of an isotropic hardening law was essential.

In this thesis, all material models adopt an associative plastic flow rule, i.e., the direction of plastic flow is normal to the yield surface. Isotropic hardening was considered only in **Paper B**, using a Voce-type law. Different yield functions and kinematic hardening evolution laws are considered throughout the thesis, which are described below.

3.2 Yield surfaces

Large plastic deformations occur in the near-surface material of rails, resulting in complex material behavior. Meyer et al. [26] employed the predeformation

technique to reproduce the large shear strains in the laboratory and demonstrated the evolution of the yield surface from an initially isotropic state to an anisotropic state with increasing predeformation. Many constitutive models have been developed in the literature to capture this evolution, often referred to as distortional hardening; see, e.g., [58–60]. Alternatively, when the objective is to describe the material response in the deformed state rather than the evolution leading to that state, the yield surface is often characterized experimentally and modeled with a fixed anisotropy; see, e.g., [61–64].

In **Paper B**, we reformulated the microstructurally motivated material model developed by Meyer and Menzel [49], accounting for evolving anisotropy with deformation, in the small-strain framework to improve its computational efficiency for the wheel over-rolling simulations. The anisotropic yield function is formulated in a quadratic form as

$$\Phi = \sqrt{\boldsymbol{\sigma}_{\text{red}}^{\text{dev}} : \hat{\mathbf{C}} : \boldsymbol{\sigma}_{\text{red}}^{\text{dev}}} - Y \leq 0 \quad \text{with} \quad \boldsymbol{\sigma}_{\text{red}}^{\text{dev}} = \boldsymbol{\sigma}^{\text{dev}} - \sum_{i=1}^{N_{\text{back}}} \boldsymbol{\beta}_i \tag{3.4}$$

Here, $\boldsymbol{\sigma}_{\text{red}}^{\text{dev}}$ is the reduced deviatoric stress, $\hat{\mathbf{C}}$ is the fourth-order anisotropy tensor, Y is the current isotropic yield limit including the isotropic hardening, and $\boldsymbol{\beta}_i$ are the back-stresses. In **Paper B**, it was assumed that there is no evolution of the anisotropy tensor, $\hat{\mathbf{C}}$, from its initial state during the short snapshot of the rail life, i.e., 348 wheel passages; see Chapter 6 for further details.

In **Papers C and D**, however, the developed frameworks for reducing the computational cost of plasticity simulations were evaluated using prototype material models based on the isotropic von Mises yield function. In this case, $\hat{\mathbf{C}}$ is replaced by $3/2\,\mathbf{I}^{\text{dev}}$ in Equation 3.4, where $\mathbf{I}^{\text{dev}}$ is the 4th order deviatoric identity tensor.

3.3 Evolution laws for kinematic hardening

Armstrong and Frederick [57] proposed a nonlinear kinematic hardening law by augmenting the linear strain hardening rule of Prager [65] with a dynamic recovery term, formulated as

$$\dot{\boldsymbol{\beta}} = -\frac{2}{3} H_{\text{kin}} \dot{\lambda} \left[-\boldsymbol{\nu} + \frac{3}{2} \frac{\boldsymbol{\beta}}{\beta_\infty} \right] \quad \text{where} \quad \boldsymbol{\nu} = \frac{\partial \Phi}{\partial \boldsymbol{\sigma}} \tag{3.5}$$

where H_{kin} is the kinematic hardening modulus, and β_∞ is the saturation value of the back-stress. Applications of the AF law for cyclic plasticity simulations of metallic materials can be found, e.g., in [66, 67]. In **Papers C and D**, this kinematic hardening law was adopted for the prototype plasticity models under multiaxial proportional loadings.

Several modifications of the AF kinematic hardening law have been proposed in the literature to address the overprediction of ratcheting (unidirectional

accumulation of plastic strains) rates; see the reviews in [68, 69]. One such modification is the second model in [70] proposed by Ohno and Wang, formulated as

$$\dot{\boldsymbol{\beta}} = -\frac{2}{3} H_{\text{kin}} \dot{\lambda} \left[-\boldsymbol{\nu} + \frac{3}{2} \frac{\boldsymbol{\beta}}{f^{\text{vM}}(\boldsymbol{\beta})} \frac{\langle \boldsymbol{\nu} : \boldsymbol{\beta} \rangle}{\beta_\infty} \left[\frac{f^{\text{vM}}(\boldsymbol{\beta})}{\beta_\infty} \right]^m \right], \tag{3.6}$$

$$f^{\text{vM}}(\boldsymbol{x}) = \sqrt{\frac{3}{2} \boldsymbol{x}^{\text{dev}} : \boldsymbol{x}^{\text{dev}}}$$

The exponent m controls the transition to saturation and, consequently, the ratcheting behavior, with smaller values of m leading to a higher ratcheting rate [69]. Moreover, the Macaulay bracket introduces different back-stress evolutions during plastic loading and unloading by activating the dynamic recovery term only when $\boldsymbol{\nu} : \boldsymbol{\beta} > 0$. In **Paper D**, the Ohno-Wang (OW) kinematic hardening law was additionally considered to assess the numerical performance of the proposed NN-based framework when using a more complex kinematic hardening law. Further applications of different variants of the OW rule can be found in the literature; for instance, Brommesson et al. [71] employed the model to account for mean stress relaxation observed in uniaxial LCF crack growth tests of high-strength titanium alloy; Skrypnyk et al. [52, 72] used it to consider ratcheting behavior in railway rail material; Lindström et al. [73] applied the first model proposed by Ohno and Wang [70] to reproduce the cyclic behavior of nickel-based superalloys subjected to uniaxial LCF loading.

Bari and Hassan [68] demonstrated that the OW kinematic hardening law overpredicts ratchetting rates under multiaxial non-proportional loading. To improve the response under such loading conditions, they followed the approach originally proposed by Delobelle et al. [74], combining the AF and Burlet-Cailleteau (BC) [75] kinematic hardening laws as

$$\dot{\boldsymbol{\beta}} = -\frac{2}{3} H_{\text{kin}} \dot{\lambda} \left[-\boldsymbol{\nu} + \boldsymbol{\nu} : \boldsymbol{\nu} \; \delta \, \frac{\boldsymbol{\beta}}{\beta_\infty} + (1 - \delta) \, \frac{\boldsymbol{\beta} : \boldsymbol{\nu}}{\beta_\infty} \, \boldsymbol{\nu} \right] \tag{3.7}$$

The material parameter δ controls the relative contributions of the AF and BC terms to the nonlinear evolution of the back-stress, $\boldsymbol{\beta}$. For the von Mises yield function, $\boldsymbol{\nu} : \boldsymbol{\nu} = 3/2$. This kinematic hardening law was employed in **Paper B**, following [49], to capture the experimentally observed material responses under non-proportional multiaxial loading.

CHAPTER 4

Considered experiments

This chapter describes the experiments considered in this thesis, namely predeformation, Low Cycle Fatigue (LCF), and High Cycle Fatigue (HCF) tests. These experiments provided the data required for the calibration and validation of the adopted and developed fatigue crack initiation criteria in **Paper A** and the anisotropic material model in **Paper B**. The predeformation tests aim to mimic the severely deformed material near the rail surface, as well as the loading conditions experienced by a rail in service. The LCF and HCF tests were further used to calibrate the models with respect to long-term cyclic and multiaxial loading.

4.1 Predeformation

Figure 4.1 shows the accumulated shear strains measured in samples extracted from the deformed railhead after 11 years in service [12]. The large shear strain gradients within the first 0.1 mm below the rail surface, particularly at the gauge corner, make conventional testing of this material difficult. Equal angular channel pressing and high pressure torsion have been used in the literature to replicate the near-surface material state. However, the extracted samples with these methods are very small for axisymmetric specimens required for multiaxial fatigue testing. Meyer et al. [12] developed an experimental technique using axisymmetric test bars in an axial-torsion machine in order to mimic the accumulation of shear strains in the surface layer of rails in the laboratory. A test bar before and after predeformation is shown in Figure 4.2, where the laser-etched lines visualize the surface shear strains. The loading condition in these experiments, i.e., combined shear and tension-compression, is similar to that experienced by rail steel during wheel-rail rolling contact [76], and surface cracks were observed during the tests. These experiments were therefore used in **Paper A** to investigate the fatigue behavior of the deformed material representing the material at a certain depth of a rail.

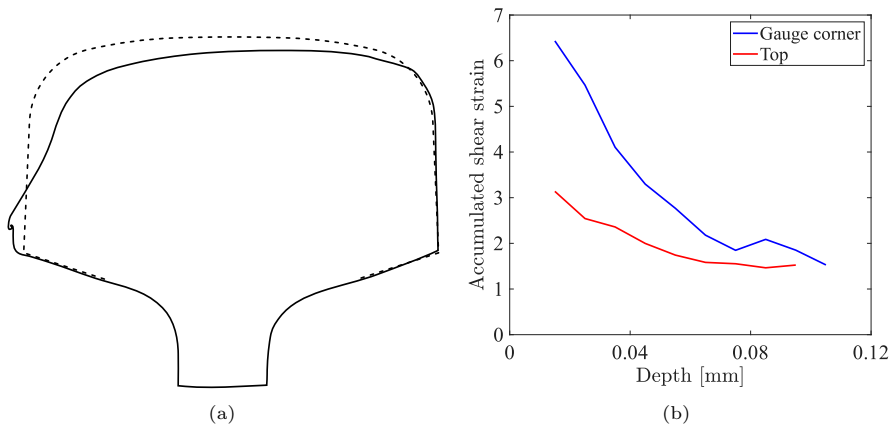


Figure 4.1: (a) Nominal 50E3 rail profile (dashed line) and deformed rail profile (solid line), and (b) measured accumulated shear strains at the gauge corner and railhead top of the deformed rail profile, from [12].

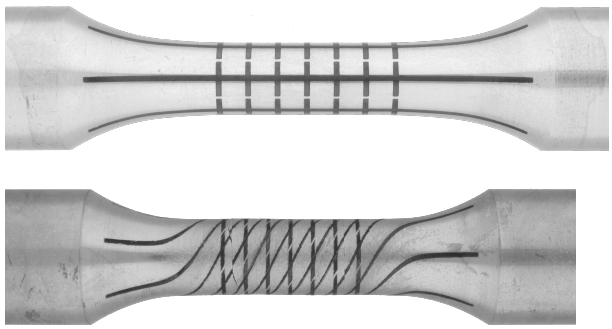


Figure 4.2: Undeformed (top) and predeformed (bottom) test bar, from [12]. The laser-etched lines visualize the surface shear strains.

4.2 Multiaxial low cycle fatigue

Due to the low number of cycles to failure in the predeformation tests, previously conducted LCF experiments were also included in the assessments of fatigue crack initiation criteria in **Paper A**. In these tests from [26], the predeformed solid test bars were subsequently remachined into thin-walled tubular shapes and were subjected to pure axial, pure shear, or proportional multiaxial loading. The majority of the fatigue life was associated with macroscopic crack initiation, and the crack propagation regime was negligible (less than 1.1% of the total life).

In **Paper B**, in addition to pure axial and pure shear test results, data from multiaxial LCF experiments with non-proportional loading, preceded by different levels of predeformation, were also considered. The resulting data

was used to calibrate and validate the anisotropic plasticity model described in Section 3.2. These experiments subjected the rail steel to pulsating compression and alternating shear, loading conditions representative of in-service wheel–rail contact [77].

4.3 Uniaxial high cycle fatigue

In **Paper A**, the experimental results from the uniaxial HCF tests conducted by Christodoulou et al. [78] on pearlitic rail steel were used as one part of the calibration dataset. The aim was to account for both HCF and LCF regimes in the J-S and the modified criteria; see Section 2.3. In [78], based on the derived S-N curve shown in Figure 4.3, the fatigue limit was identified as 540 MPa at a fatigue life of 10^7 cycles. This fatigue limit, together with the stress ratio of 0.1, was used in the calibration procedure in **Paper A**.

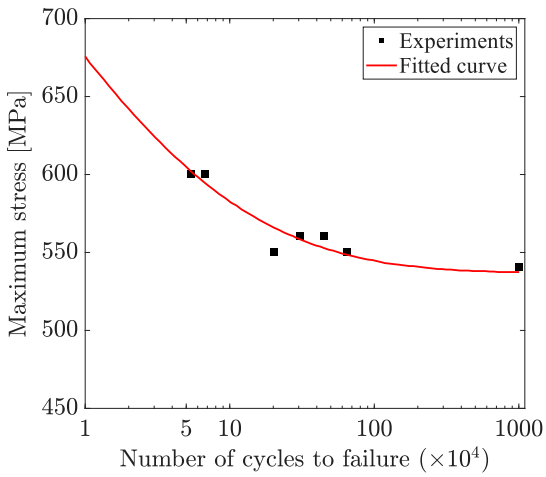


Figure 4.3: Fatigue S-N curve, regenerated from [78].

CHAPTER 5

Parameter identification using experimental data

Connecting advanced models with experimental data through parameter identification formed one important part of the work carried out in the first two papers of this thesis. In **Paper A**, numerical optimization was used to identify the fatigue parameters of the crack initiation criteria, while in **Paper B**, it was used to identify the material parameters of the adopted plasticity model.

A general optimization problem involves finding an optimal solution $\boldsymbol{x}_{\text{opt}}$ that minimizes an objective function $f(\boldsymbol{x})$

$$\boldsymbol{x}_{\text{opt}} := \arg \underset{\boldsymbol{x} \in S}{\text{minimum}}\ f(\boldsymbol{x}), \tag{5.1}$$

where $S \subseteq \mathbb{R}^n$ is a nonempty set, $\boldsymbol{x} \in \mathbb{R}^n$ is a vector of model parameters with components x_j, $j = 1, ..., n$, and $f : \mathbb{R}^n \to \mathbb{R}$. Techniques for solving optimization problems can be broadly divided into two groups: derivative-free methods, such as the Nelder-Mead simplex algorithm [79], BOBYQA [80], and particle swarm optimization, and gradient-based methods, such as steepest descent, Newton's method, Levenberg-Marquardt [81], and the Rectified Adam (RAdam) optimizer [82]. Using the Nelder-Mead simplex algorithm with multiple initial guesses has been successfully applied in previous studies; see, e.g., [56, 83], and it was thus also adopted in **Papers A and B**. The algorithm was employed to minimize the objective function of a least-squares type, which, in general, is formulated as

$$f(\boldsymbol{x}) = \left|\left| \boldsymbol{y}^{\text{exp}} - \boldsymbol{y}^{\text{sim}}(\boldsymbol{x}) \right|\right| \tag{5.2}$$

where $\boldsymbol{y}^{\text{exp}}$ denotes experimental data, and $\boldsymbol{y}^{\text{sim}}(\boldsymbol{x})$ denotes the corresponding simulated data from the model (as a function of the model parameters, $\boldsymbol{x}$). The general parameter identification procedure adopted in **Papers A and B** is summarized as follows:

1. Define lower and upper bounds $\boldsymbol{x}_{\text{min}}$ and $\boldsymbol{x}_{\text{max}}$ for the parameters $\boldsymbol{x}$, thereby specifying the admissible parameter space $\Omega = \{\boldsymbol{x} \,|\, \boldsymbol{x}_{\text{min}} \leq \boldsymbol{x} \leq \boldsymbol{x}_{\text{max}}\}$.

2. Generate a full set S_{full} of initial guesses $\boldsymbol{x}$ within the parameter space Ω using Latin hypercube sampling.
3. In **Paper A**, retain S_{full}. In **Paper B**, evaluate the objective function for all initial guesses in S_{full}, and choose those with the lowest objective function values to form a reduced set S_{red}.
4. Perform numerical optimization from each selected initial guess to minimize the objective function $f(\boldsymbol{x})$.
5. Select the k best-optimized parameter sets with the lowest objective function values, resulting in the updated set S_{red}. Pass these as initial guesses (updated $\boldsymbol{x}$) to the subsequent optimization step.
6. Reduce k
7. Repeat steps 4 to 6 until convergence.

In **Paper A**, the objective function minimized the difference between the fatigue crack initiation lives from the experiments and numerical predictions. An observed issue with the Nelder-Mead simplex algorithm was its tendency to converge to solutions at the lower or upper bounds of the parameter intervals. To mitigate this and improve the robustness of the optimization procedure, sufficiently wide permissible parameter intervals were used. The quality of a model cannot be evaluated only by its ability to fit experimental data, as considering more independent model parameters may improve the fit but reduce the model's predictive ability (i.e., overfitting). Accordingly, in **Paper A**, a one-fold cross-validation [84] was employed to assess the performance of each crack initiation criterion on new data and to mitigate the risk of overfitting. This method involves dividing the experimental dataset (with size p) into calibration data (with size $p-1$) and validation data (with size 1) in p possible ways.

In **Paper B**, to achieve a material model capable of describing the material behavior in a railhead under in-service conditions, the parameters of the adopted anisotropic plasticity model were calibrated against experimental data at different predeformation levels, each characterized by a certain amount of accumulated shear strain. Specific experiments were used to identify particular material parameters, thereby reducing the complexity of the optimization procedure; see e.g. [85]. Young's and shear moduli were determined from the mean values of the elastic moduli during the pure axial and pure shear loading experiments, respectively. The initial back-stress, corresponding to the center of the yield surface after predeformation, was optimized against the monotonic parts of the first loading cycles from four uniaxial LCF experiments with different loading directions. The remaining material parameters were identified using a step-wise approach. In summary, a set of optimized parameters with the lowest objective function values was chosen as the initial guesses for the subsequent optimization step. This strategy was intended to guide the optimization algorithm towards finding the optimal solution. Moreover, some experimental data were retained to evaluate the performance of the plasticity model on unseen data.

CHAPTER 6

Framework to predict fatigue crack initiation in highly deformed rail steel

The goal of **Papers A and B** was to further enhance simulation-based RCF crack initiation predictions by evaluating the importance of accounting for deformation-dependent material behavior and changes in rail profile geometry. This led to the development of a framework, an overview of which is presented in Figure 6.1. First, LCF experiments with railway-like loading, following different levels of predeformation, were used to calibrate an anisotropic plasticity model (a and b). The calibrated model parameters, together with the reconstructed distribution of accumulated shear strains in the railhead, were then used to introduce spatially varying material properties (c). Subsequently, FE simulations of wheel over-rollings were performed to obtain local stress and strain histories in railheads with different combinations of material states and profile geometries under mixed traffic loading (d). Finally, the fatigue crack initiation criterion developed in **Paper A** was applied to evaluate the accumulated RCF damage after the load sequence in the railheads (e). The following sections describe the specific methods, assumptions, and modeling choices adopted for each component of the framework. Note that the experiments used in this Chapter are described in Chapter 4.

6.1 Material model calibration

To account for deformation-dependent material behavior, the plasticity model adopted in **Paper B** with the anisotropic yield surface defined in Equation 3.4 was calibrated against the multiaxial LCF experiments preceded by different levels of predeformation. In addition to the undeformed case (PD_0), cyclic tests following 1 (PD_1), 3 (PD_3), and 6 (PD_6) predeformation cycles were included in the calibration. These predeformation levels induced surface shear strains of 0.21, 0.60, and 1.13, respectively. The calibration procedure (briefly described in Section 5) included 1 experiment for PD_0 and 3 experiments for each of the predeformation levels PD_1 to PD_6, with the cycle numbers ranging from 660 to 2108. These cycle numbers were chosen to ensure that fatigue-induced

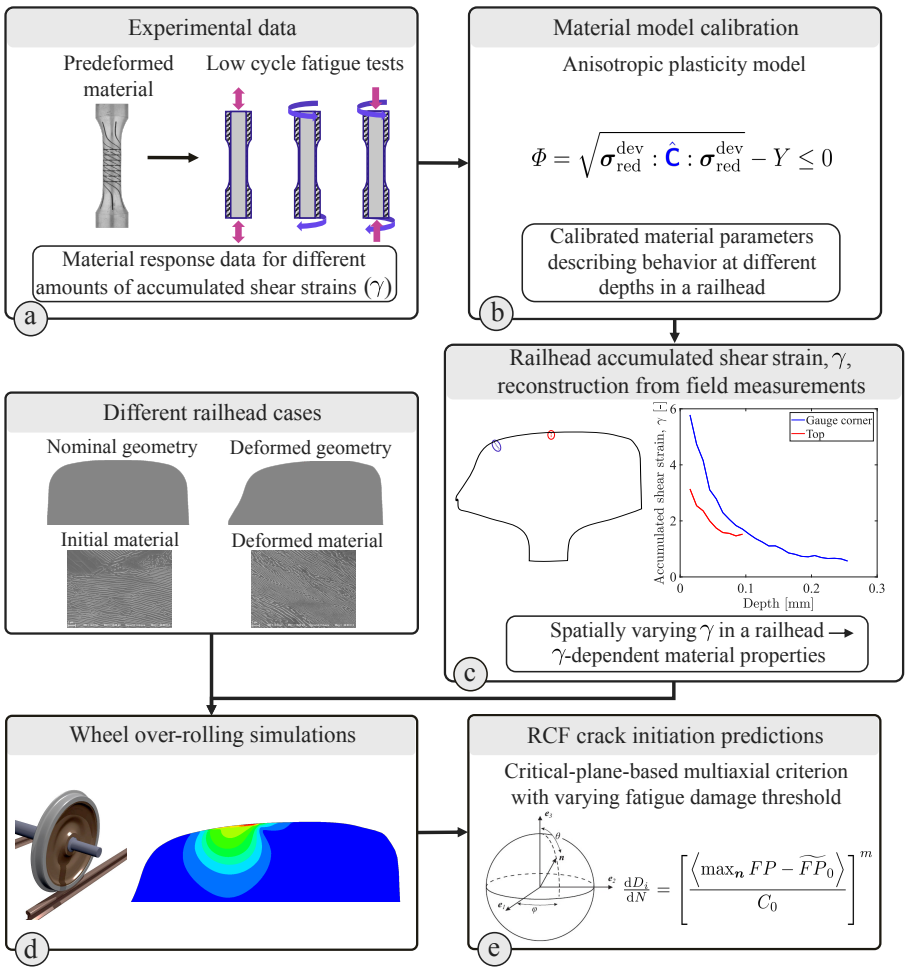


Figure 6.1: The framework developed in **Paper B** for RCF crack initiation predictions in highly deformed railheads.

softening had not influenced the stress amplitudes.

As presented in Figure 6.2, the experiments show increased hardening with increasing predeformation in both cycle 1 and 100, particularly between PD_0 and PD_1. The calibrated material model captures this trend well in both the axial and shear responses. Despite some over- and underestimation of the stress responses, the overall agreement with the experiments is very good, especially considering the complexity of the non-proportional multiaxial loading and the large number of loading cycles included in the optimization.

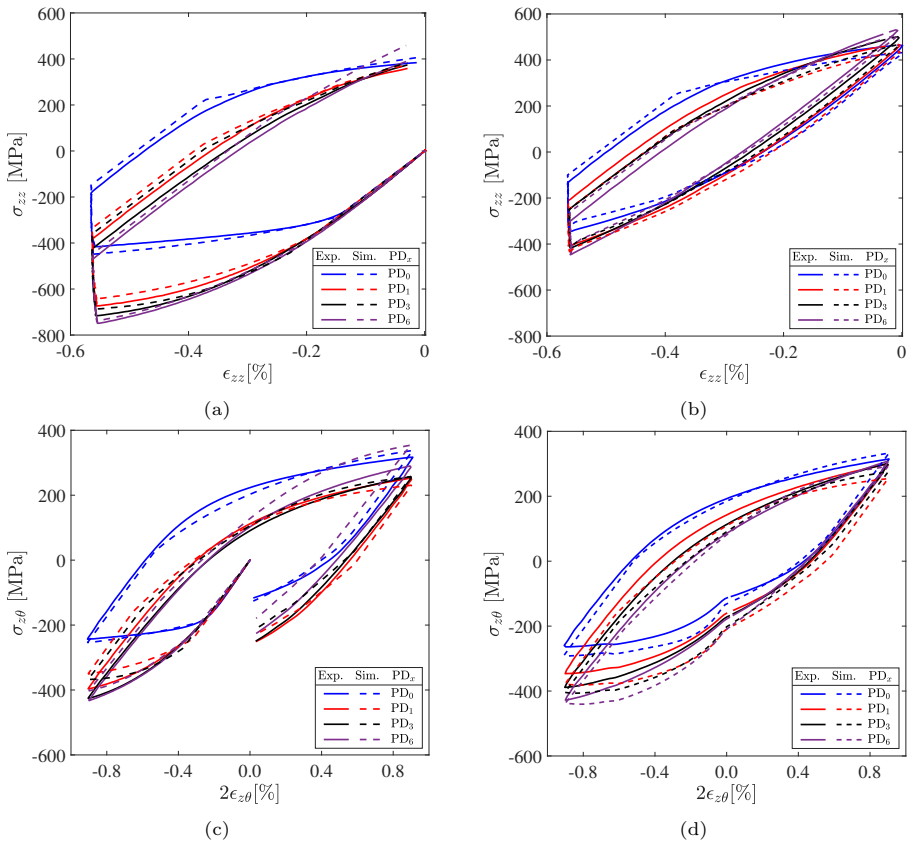


Figure 6.2: Calibrated stress-strain responses from **Paper B** for the axial direction: (a) cycle 1 and (b) cycle 100, and for the shear direction: (c) cycle 1 and (d) cycle 100. Exp. and Sim. denote the experimental and simulation results, respectively. PD$_x$ refers to x cycles of predeformation.

6.2 Distribution of accumulated shear strains and anisotropy in railhead cross-section

Wheel-rail contact generates high contact stresses, resulting in the heterogeneous accumulation of large shear strains in the railhead over long-term service [7]. In **Paper B**, the spatial distribution of the accumulated shear strains, γ, in field samples was reconstructed based on measurements from [12]. Figure 6.3 illustrates the resulting distribution in the cross-section of a worn rail profile. At points P_1 and P_4, γ was assumed to be zero at all depths, and, between these points, linear interpolation considering the measurements at points P_2 and P_3 was performed in the $\xi - \eta$ coordinate system. The distribution shows that γ decreases with depth and also varies in the transverse direction.

Next, the material parameters and anisotropy tensors, $\hat{\mathbf{C}}$, identified for

different predeformation levels (see Sections 6.1 and 6.3.1), each corresponding to a specific accumulated shear strain, were used to introduce spatially varying material properties in the railhead. Specifically, based on the value of γ at a given spatial position, the material properties were determined using linear interpolation between properties for the predeformation levels. This results in a unique material model parameters at each integration point in the railhead.

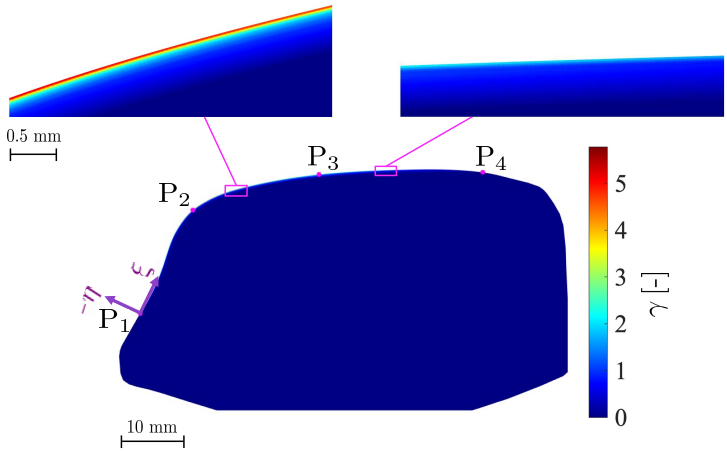


Figure 6.3: Reconstructed distribution of the accumulated shear strain, γ, over the railhead cross-section.

6.3 FE simulations

6.3.1 2D axisymmetric simulations of predeformations

For calibrating the fatigue crack initiation criterion developed in **Paper A** and adopted for the evaluations in **Paper B**, the predeformation tests from [12] were considered as one of the calibration datasets. During these tests, however, shear strain varies radially, resulting in inhomogeneous stress and strain fields within the specimen. Consequently, only the axial force, the specimen's elongation, torque, and twist were measured in the experiments [12]. To obtain the local stress and strain histories, 2D axisymmetric FE simulations of the predeformation tests and the predeformation parts of the LCF tests were performed in Abaqus [86] in **Paper A**. Moreover, in **Paper B**, the anisotropy tensors, $\hat{\mathbf{C}}$, for each predeformation level were extracted from the FE simulations of the predeformation tests considered in that paper. These simulations employed the finite strain model formulation in [49], accounting for distortional hardening through the evolving anisotropy tensor $\hat{\mathbf{C}}$. Figure 6.4 shows the distribution of the shear stresses before unloading in the 6^{th} predeformation cycle under a nominal compressive stress of -600 MPa. The shear stress, $\sigma_{z\theta}$, increases in the radial direction from the center to the surface of the test bar, while no

gradient in the axial direction in the gauge section can be observed.

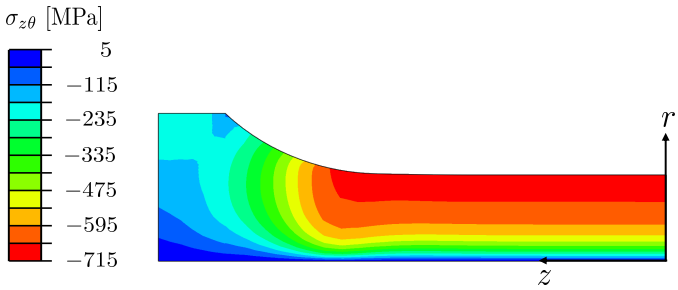


Figure 6.4: Shear stresses in the 6$^{\text{th}}$ predeformation cycle, before unloading, at the nominal compressive stress of −600 MPa.

6.3.2 Wheel over-rolling simulations

FE simulations of wheel–rail contact situations in the literature range from detailed 3D FE models to computationally efficient 2D formulations. The former provide a comprehensive representation of the rolling contact problem by resolving the full 3D stress and strain fields; see, e.g., [77, 87–92]. However, they are computationally demanding when simulations require a finely resolved railhead mesh, advanced cyclic plasticity models, a fine time discretization of each loading cycle, and a large number of wheel passages. To address this, several approaches have been developed in the literature. Some studies have proposed computationally efficient 3D FE formulations aimed at retaining the complexity of rolling contact conditions while lowering the computational costs [53, 93]. An alternative approach is to use simplified 2D plane strain FE formulations, such as those used in [52, 94, 95], which are more computationally efficient, but significantly approximate the contact stress distributions. A further alternative is a 2D Generalized Plane Strain (GPS) FE model of the rail cross-section developed in [96], which accounts for the out-of-plane axial and bending stiffness of the rail. This model was shown to reproduce the results of the corresponding full-scale 3D model with good accuracy and a noticeable reduction in the computational time [96].

Resolving the large shear strain gradients close to the rail surface in **Paper B** required a very fine mesh. To simulate wheel over-rollings at a reasonable computational cost, the 2D GPS framework from [96] was adopted. In the implementation of the GPS model in Abaqus [86], the 2D cross-section has a constant curvature in the longitudinal direction of the rail and is positioned between two rigid bounding planes. These planes can translate axially and rotate around the in-plane axes with respect to a reference point. In [96], to mimic a Hertzian contact pressure distribution moving longitudinally, the element thicknesses were scaled such that the variation of the maximum von Mises stresses in the 2D GPS model matches those from the corresponding 3D model.

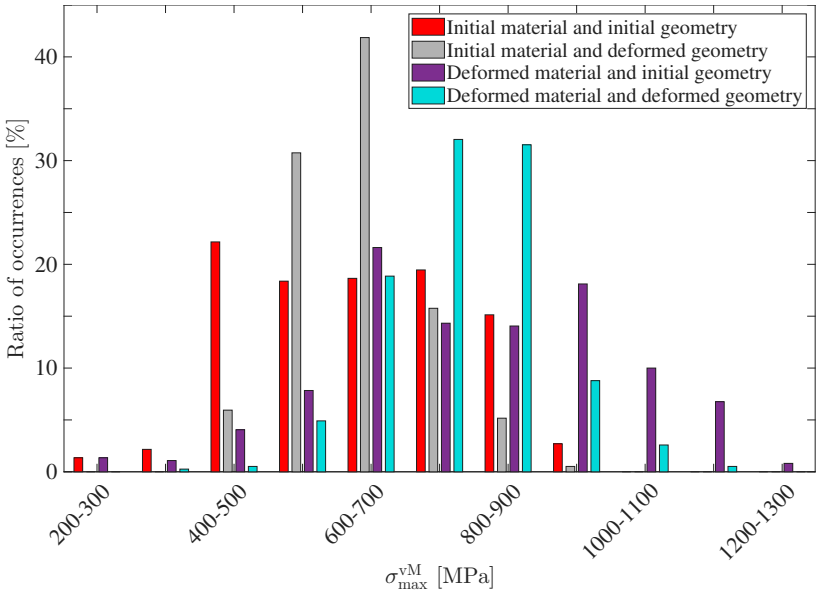


Figure 6.5: Distributions of maximum von Mises stresses, $\sigma_{\max}^{\mathrm{vM}}$, from **Paper B**.

In the wheel over-rolling simulations of **Paper B**, the railheads were subjected to a mixed traffic loading obtained from the simulation methodology in [97] for a curved track located at the west mainline in Sweden between Nyckelsjön and Sparreholmen. The load sequence comprises 348 wheel passages, representing 20 passenger trains with axle loads ranging from 11.7 to 21.0 tonnes, 279 different measured wheel profiles, and varying vehicle speeds. In **Paper B**, a full-slip condition with a traction coefficient of 0.4 was assumed to represent a severe loading condition for the development of surface RCF damage. According to the shakedown map [6], surface-initiated RCF damage, which is the focus of **Paper B**, is associated with traction coefficients larger than approximately 0.3. After an evaluation of different traction coefficients, a value of 0.4 was adopted, which can represent dry wheel-rail interfacial conditions according to field measurements [98].

The over-rolling simulations in **Paper B** considered four distinct railhead cases, combining either initial or deformed material with either initial or deformed geometry. Initial material and geometry refer to homogeneous virgin (isotropic) material and a nominal rail profile in this study. Figure 6.5 presents the frequency of occurrences of the maximum von Mises stresses, $\sigma_{\max}^{\mathrm{vM}}$, over all wheel passages for the four railhead cases. The results show that the railheads with deformed and hardened material experience higher values of $\sigma_{\max}^{\mathrm{vM}}$ compared to the railheads with initial material. In contrast, the deformed rail geometry reduces the frequency of load cases causing high $\sigma_{\max}^{\mathrm{vM}}$. These results demonstrate the importance of accounting for the material state and rail profile geometry when evaluating the mechanical response of rails.

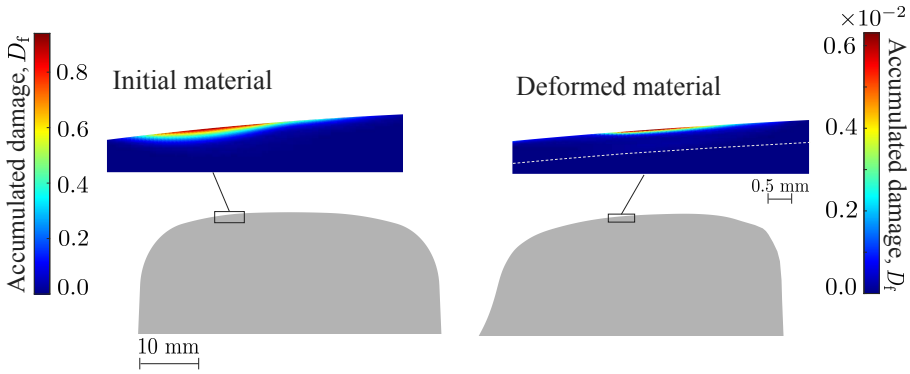


Figure 6.6: Accumulated damage for the railheads after the load sequence. The depth of the deformed layer is assumed to be 0.5 mm, as indicated by the dashed lines.

6.4 RCF damage predictions

In the final step of the framework, the fatigue crack initiation criterion developed in **Paper A** (see Section 2.3), which accounts for the influence of plastic deformations, was employed to examine the effect of material state and rail profile geometry on the fatigue performance of the railheads. For the railheads with deformed near-surface material, the initial ratcheting strain, ϵ_r, at each integration point was assumed to be a function of γ. Accordingly, the initial ϵ_r was obtained by linear interpolation of the ratcheting strains from the FE simulation results of the predeformation tests.

Table 6.1 presents the maximum accumulated LCF damage after the load sequence for the four railheads. The results show that both the deformed near-surface material and deformed geometry significantly reduce the accumulation rate of fatigue damage. When the effects of deformed material and geometry are considered simultaneously, the predicted fatigue damage is reduced by a factor of about 150 compared with the case with initial material and geometry. The corresponding spatial distributions of the accumulated fatigue damage, D_f, in the highly damaged regions are shown in Figure 6.6. The spatial damage gradient in both railheads is very large, with the maximum D_f occurring very close to the surface. These results from **Paper B** underline the significant influence of material state and rail profile geometry changes on RCF damage predictions, as neglecting these effects can lead to considerable overestimation.

Table 6.1: Maximum per-sequence accumulated damage, $D_{f,\,max}$, in the railheads.

Railhead cases	$D_{f,\,max}$
Initial geometry and initial material	0.940
Initial geometry and deformed material	0.185
Deformed geometry and initial material	0.026
Deformed geometry and deformed material	0.006

CHAPTER 7

Machine Learning (ML)-based approaches to accelerate plasticity simulations

7.1 Motivation and introduction

The field samples mentioned in Section 4.1 were extracted from the main railway line between Stockholm and Gothenburg in Sweden. Traffic on this line is dominated by passenger trains with axle loads ranging from 15 to 19 tonnes. The annual traffic is in the order of $15 \cdot 10^6$ tonnes, resulting in about 10^6 wheel passages per year. Reproducing such loading histories in FE simulations is computationally expensive, particularly when nonlinear constitutive models are employed, as required in simulations aiming at predicting plasticity-induced fatigue crack initiation in rails [77, 87, 90, 92, 99]. In such simulations, each cycle must be resolved into a sufficient number of time steps. In each time increment, the Differential Algebraic Equations (DAEs) of the nonlinear material model must be solved at every integration point in the FE mesh during each equilibrium iteration. Therefore, developing methods that address the computational cost associated with the large number of loading cycles and repeated evaluation of the nonlinear constitutive equations can reduce the cost of such simulations.

For plasticity simulations involving a large number of loading cycles, one way to reduce the computational cost is to decrease the number of loading cycles that need to be explicitly simulated. Cycle jumping is one such approach, based on the observation that, although stresses and strains may vary strongly within an individual loading cycle, their evolution from one cycle to the next is often slower. Instead of resolving every cycle, selected cycles are simulated, and the state variables (and global responses) are extrapolated over several intermediate cycles; see, e.g., [100–104]. An alternative way of reducing the number of explicitly simulated cycles is the approach proposed by Brommesson et al. [71]. For cyclic plasticity simulations involving gradual mean-stress relaxation, they scaled the number of cycles in the experiments and calibrated the material model parameters accordingly.

In these approaches, a time-domain model is retained, and its solution is extrapolated over intermediate cycles. A different strategy is to reformulate the material model itself in the cycle domain. This approach, which was adopted in **Paper C** and will be described in more detail in Section 7.2, presents the challenge of formulating suitable per-cycle evolution laws for the state variables, such as the plastic strain. Following conventional phenomenological material modeling, one can choose an analytical ansatz and incorporate experimental observations and physics into it, followed by calibration of the model parameters. However, this approach relies on experiments, which are very expensive to conduct.

Another approach to formulating the per-cycle evolution laws is to use ML methods. ML has found applications across a wide range of disciplines, including constitutive modeling [105], where it has shown potential for improving the accuracy and computational efficiency of material models; see, e.g., the review in [16]. ML-based constitutive modeling can be divided into uninterpretable and interpretable approaches [16]. Uninterpretable approaches, which include artificial Neural Networks (NNs), represent an input-output mapping that cannot be physically explained. In early NN-based constitutive modeling, they were used to approximate mappings from strain, strain history, or state variables to stress or state-variable increments [106–110]. Although such models can represent nonlinear and history-dependent behavior, their predictive capability outside the training regime is generally low, as they are unaware of the underlying physics [111]. The inclusion of physics in NN-based constitutive modeling has been shown to noticeably improve generalization [112].

Adherence to physical constraints can be addressed either weakly through the training procedure or strongly through the model formulation. For instance, inspired by the idea of Physics-Informed Neural Networks (PINNs) [113], Haghighat et al. [114] proposed a PINN-based constitutive modeling framework in which violations of elastoplastic inequality constraints were penalized in the loss function. Weber et al. [115] extended the idea of constrained NNs in [116] to rate-independent plasticity by enforcing physical constraints, such as material tangent symmetry and material stability, via error terms in the loss function. Despite their impressive ability to describe material behavior, these approaches do not guarantee physical constraints by construction. Instead, these constraints are only weakly enforced in the loss function during training. In contrast, in [117], Feed Forward Neural Networks (FFNNs) were embedded directly into the evolution equations for internal variables. Independent of the training, their formulation intrinsically satisfied physical requirements. Using an alternative approach, Fuhg et al. [118] introduced a thermodynamically consistent framework based on isotropic and nonlinear kinematic hardening potentials, and following this, Jadoon et al. [119] developed an NN-based framework for finite strain elastoplastic material modeling.

In contrast to uninterpretable approaches, interpretable ML-based models aim to identify explicit mathematical relationships from data, thereby facilitating the interpretation of model parameters and their influence on the material response. Techniques such as sparse regression [117, 120–122] and Symbolic

Regression (SR) have been applied to constitutive modeling. SR, which often refers to methods based on genetic algorithms [16], does not require a priori assumptions of functional forms. Instead, only building blocks such as mathematical operators, functions, and numerical constants need to be defined [123]. Applications include the discovery of flow stress equations for copper [124], the von Mises yield function and plastic strain evolution equation [125], and strain-energy density functions for hyperelastic materials [126]. Adherence to physical constraints has also been investigated. For instance, Foroughi Boroujeni et al. [127] enforced the second law of thermodynamics during training by penalizing violating symbolic expressions for hypoplasticity. Garbrecht et al. [128] combined a continuum thermodynamic analysis with SR to identify the Gurson yield function for porous materials, with physically derived requirements incorporated either as fitness criteria or directly enforced in the symbolic formulation. A disadvantage of symbolic regression is its long training time and the lack of guaranteed convergence to an accurate expression [16, 129]. Another challenge is that restricting the complexity of the discovered expressions to preserve interpretability can limit their expressiveness. To address this trade-off, for instance, in [130], the expressiveness of Kolmogorov-Arnold networks was combined with the interpretability of symbolic models to find the strain energy function of isotropic hyperelastic materials from experimental data.

In addition to extensive research advancing ML-based constitutive modeling, recent studies have developed ML-based methods to mitigate or alleviate the computational bottleneck of repeatedly evaluating nonlinear equations at the material point level. Some methods replace the stress-update algorithm with data-driven surrogates, learning plasticity constraints primarily from data [131–134]. To enhance generalizability, some approaches employ PINN-based surrogates in which physical constraints are enforced through the loss function [17, 135]. Rather than replacing the entire constitutive update with a surrogate, Li et al. [136] proposed a PINN-driven framework that bypasses only the local stress integration procedure, and the consistency condition error was incorporated into the training loss function. In [18], an NN was used to predict the stress increment during plastic loading, while residuals of the stress update and the consistency condition were included in the loss function. A different strategy was proposed by Malleval et al. [19], who employed NNs to facilitate finding the solution of a scalar local nonlinear equation. In contrast to these approaches, in **Paper D**, a physics-encoded framework for speeding up the time integration of nonlinear constitutive equations allowing very large strain increments was proposed, which will be described in Section 7.3.

7.2 ML-based cycle-domain plasticity modeling

In a cycle-domain model, a time-domain material model is formulated in the cycle domain such that cycle number N, rather than time t, becomes the evolution variable. Suiker and de Borst [137] proposed such an approach for long-term accumulation of plastic deformations in ballasted railway tracks. Their

model's framework builds upon standard plasticity theory and is formulated as a viscoplastic model where the rates of the variables are described as their change per unit cycle N. The per-cycle evolution of plastic strain is governed by an overstress formulation, where plastic strain develops when the stress amplitude in a given load cycle exceeds a certain threshold value. Using this model, Li et al. [138] developed a 3D FE simulation framework to predict the ballasted railway track settlement in a crossing panel subjected to many wheel passages. The cycle-domain modeling approach has also been applied to formulating the fatigue damage model of short-fiber reinforced plastics, such as in the studies by Köbler et al. [139] and Magino et al. [140]. More recently, Dey et al. [141] incorporated a logarithmic cycle-domain formulation into a multiscale, data-driven modeling framework for short-fiber reinforced plastics.

7.2.1 Formulation

The cycle-domain modeling approach adopted in **Paper C** is schematically illustrated in Figure 7.1. For a given pulsating uniaxial strain history (top figure), the model predicts the peak stress and the corresponding plastic strain (bottom figure) in each cycle N, denoted by ${}^{N}\sigma_{11}$ and ${}^{N}\epsilon^{\mathrm{p}}_{11}$, respectively. In the implementation considered in **Paper C**, the first half-cycle is simulated using the reference time-domain material model, after which the subsequent cycles are predicted using the cycle-domain model.

As mentioned, in a cycle-domain formulation, time derivatives of quantities are replaced with their changes per unit cycle N. Accordingly, suitable evolution laws are required to describe the evolution of the state variables per loading cycle. In **Paper C**, FFNNs and SR were employed to formulate such an evolution law for the plastic strain. Specifically, an ML model, f_{ml}, was trained to predict the per-cycle evolution of the plastic strain, $\mathrm{d}^{N}\epsilon^{\mathrm{p}}_{11}/\mathrm{d}N$, from cycle $N-1$ to N, formulated as

$$\frac{\mathrm{d}\sigma_{11}}{\mathrm{d}N} = E\,\frac{\mathrm{d}\epsilon^{\mathrm{e}}_{11}}{\mathrm{d}N} = E\left[\frac{\mathrm{d}\epsilon_{11}}{\mathrm{d}N} - \frac{\mathrm{d}\epsilon^{\mathrm{p}}_{11}}{\mathrm{d}N}\right] \tag{7.1}$$

$$\frac{\mathrm{d}^{N}\epsilon^{\mathrm{p}}_{11}}{\mathrm{d}N} = \mathcal{H}_{\Phi}\left({}^{N-1}\epsilon^{\mathrm{p}}_{11},\, {}^{N}\sigma^{\mathrm{tr}}_{11}\right) f_{\mathrm{ml}}\left(\boldsymbol{x}\right) \qquad \text{where} \tag{7.2}$$

$$\mathcal{H}_{\Phi}\left({}^{N-1}\epsilon^{\mathrm{p}}_{11},\, {}^{N}\sigma^{\mathrm{tr}}_{11}\right) = \begin{cases} 0, & \text{if } {}^{N-1}\epsilon^{\mathrm{p}}_{11} = 0 \quad \text{and} \quad |{}^{N}\sigma^{\mathrm{tr}}_{11}| < Y_0 \\ 1, & \text{otherwise} \end{cases} \qquad \text{and}$$

$${}^{N}\sigma^{\mathrm{tr}}_{11} = E\left[{}^{N}\epsilon_{11} - {}^{N-1}\epsilon^{\mathrm{p}}_{11}\right]$$

where E is Young's modulus. $\mathcal{H}_{\Phi}(\cdot)$ suppresses plastic strain evolution when the material response is purely elastic (no previous plasticity). A semi-implicit discretization scheme was used between consecutive loading cycles.

The ML models were initially evaluated using two input features, $\boldsymbol{x} = \{{}^{N}\sigma_{11},\, {}^{N-1}\epsilon^{\mathrm{p}}_{11}\}$. Analysis of the training data, however, showed that nearly the same inputs could correspond to different values of the plastic strain increment, resulting in a non-unique input-output mapping. To provide additional

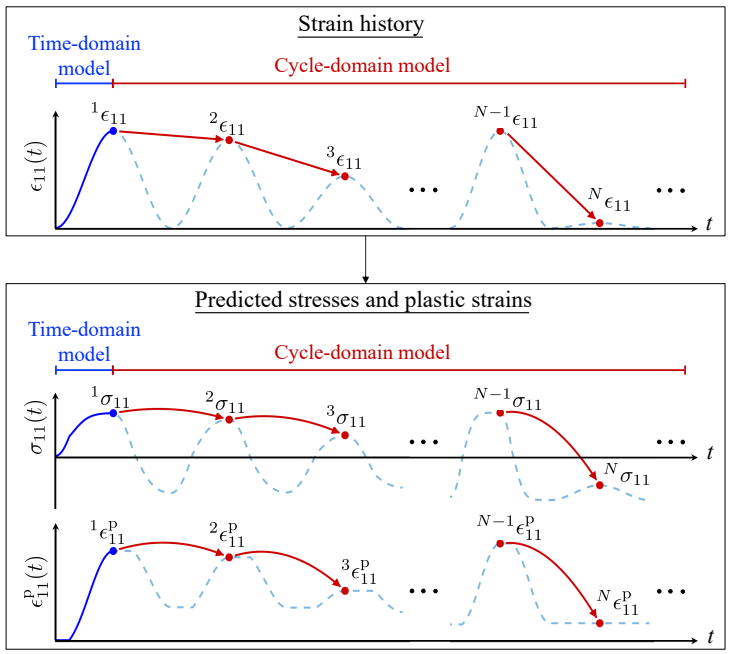


Figure 7.1: Schematic illustration of the cycle-domain material model in cyclic simulations, from **Paper C**. The solid blue lines represent the input strain history to the time-domain model and its simulated first half-cycle. The red circles show the peak strain ${}^{N}\epsilon_{11}$, as well as the peak normal stress ${}^{N}\sigma_{11}$ and the corresponding plastic strain ${}^{N}\epsilon^{\mathrm{p}}_{11}$ predicted by the cycle-domain model for the loading cycle N. The dashed light blue lines denote the strain histories and responses from the time-domain model.

information about the loading history, the peak stress from the previous cycle, ${}^{N-1}\sigma_{11}$, was introduced as a third input. This lowered the training, validation, and test losses and improved the predictive accuracy of the cycle-domain model.

7.2.2 Numerical performance evaluation

Figure 7.2 illustrates the procedure in **Paper C** to obtain and evaluate the cycle-based evolution law for the plastic strain, $\mathrm{d}^{N}\epsilon^{\mathrm{p}}_{11}/\mathrm{d}N$. The FFNN's parameters, i.e., weights and biases, were identified using the RAdam optimizer in the open-source PyTorch library [142]. SR was performed using the open-source PySR library [143], employing an evolutionary algorithm based on genetic programming. Further details regarding the training are provided in **Paper C**.

Figure 7.3(a) shows the predicted stresses and plastic strains during the last 100 cycles of a 5000-cycle simulation using the NN-based cycle-domain model. Although the NN was trained on loading sequences containing only 100 cycles, close agreement was achieved with the reference time-domain model. After 5000 cycles, the mean absolute error in σ_{11} was 10.1 MPa, and the relative error in $\epsilon^{\mathrm{p}}_{11}$ was 0.68%. Moreover, extending the simulation to 10000 cycles did

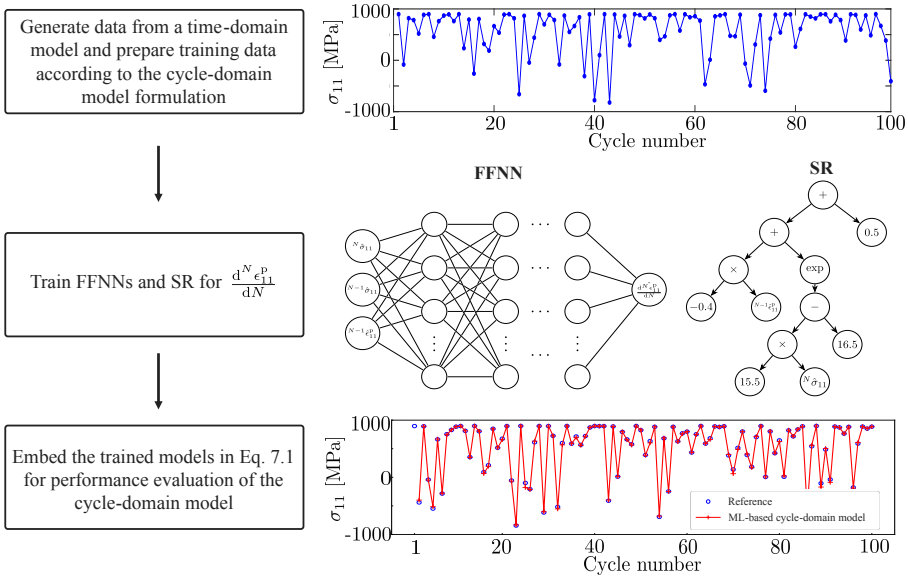


Figure 7.2: The procedure used in **Paper D** to obtain and assess the per-cycle evolution law for the plastic strain, $\mathrm{d}^N\epsilon^{\mathrm{p}}_{11}/\mathrm{d}N$.

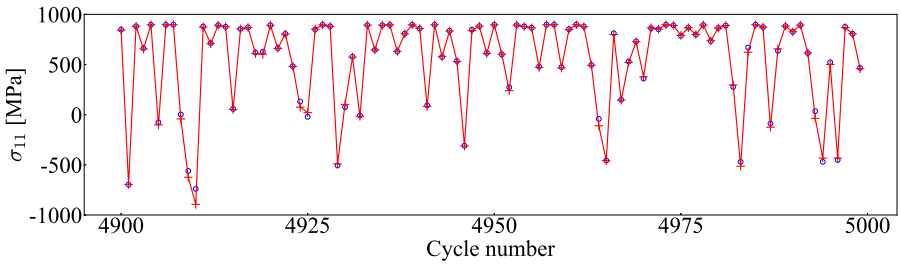
not result in noticeable error accumulation in either σ_{11} or $\epsilon^{\mathrm{p}}_{11}$.

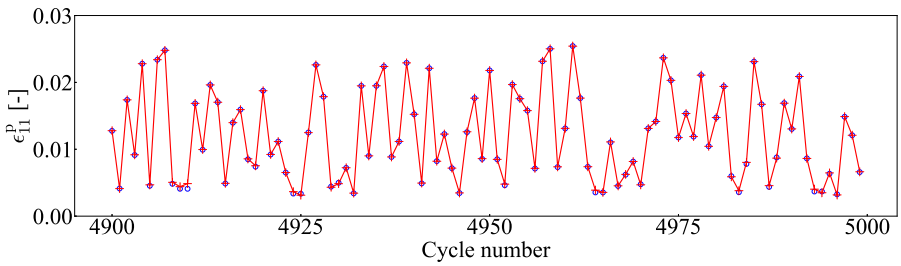
Regarding the SR-based model, the most accurate symbolic expression discovered was

$$f_{\mathrm{sr}}({}^N\hat{\sigma}_{11}, {}^{N-1}\hat{\sigma}_{11}, {}^{N-1}\hat{\epsilon}^{\mathrm{p}}_{11}) = \Big[\exp(167.36\,{}^N\hat{\sigma}_{11} - 168.91) + 0.46 - \tanh\Big(\tanh\Big(\tanh\big(0.08\exp(2\,{}^{N-1}\hat{\epsilon}^{\mathrm{p}}_{11})\big) ({}^{N-1}\hat{\sigma}_{11})^2\big)\Big)\Big] + 1.23\times10^{-4}\exp\Big(\exp({}^N\hat{\sigma}_{11} + 1.04)\Big) \tag{7.3}$$

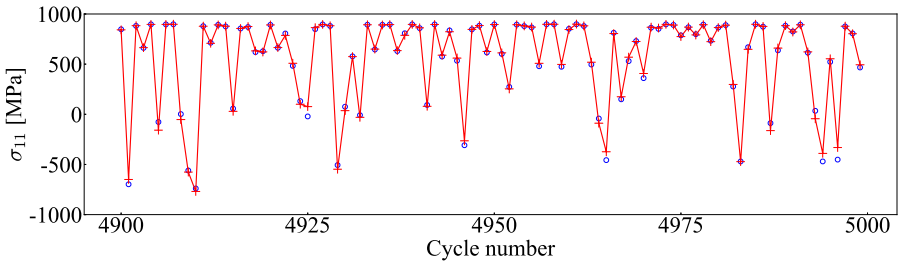
Here, $\hat{\bullet}$ denotes min-max normalized variables. Although the resulting expression is explicit and human-readable compared with the black-box NN, its relatively high complexity limits its interpretability, showing a trade-off between accuracy and interpretability. Figure 7.3(b) presents the predicted stresses when the expression above was employed as the per-cycle evolution law for the plastic strain in the cycle-domain model formulation, showing very good agreement with the reference results. In particular, the simulation of 5000 loading cycles resulted in a mean absolute error of 14.8 MPa in σ_{11}, which is comparable to that obtained with the NN-based cycle-domain model.

The results of **Paper C** demonstrated that both the NN- and SR-based cycle-domain models can provide accurate predictions even far beyond the training regime. However, the ML-based cycle-domain models required a large amount of training data to learn the results from the time-domain model.





(a) NN



(b) SR

Figure 7.3: Stress versus cycle number and plastic strain versus cycle number over 5000 loading cycles when employing the NN and SR models in the cycle-domain model formulation, from **Paper C**. Only the last 100 loading cycles are shown. Circles and red plus signs correspond to the results from the time-domain model and the cycle-domain model, respectively.

7.3 ML-accelerated time integration of small-strain plasticity models

As mentioned previously, in addition to reducing the computational cost of cyclic simulations by reformulating constitutive models in the cycle domain, computational efficiency can also be improved by accelerating the time integration of time-domain plasticity models. The explicit forward Euler time integration scheme is computationally fast, but requires small time increments to preserve numerical stability [144]. The backward Euler time integration scheme permits larger increments but typically requires the iterative solution of nonlinear equations.

Considering the literature on ML-based acceleration of the numerical integration of plasticity models reviewed in Section 7.1, although most of them helped reduce the cost of iteratively solving the nonlinear equations, they did not inherently satisfy fundamental plasticity constraints in their formulations. This was addressed in **Paper D** by retaining essential parts of the underlying plasticity formulation in analytical form and employing NNs to construct an explicit time integrator for the evolution of the state variables.

7.3.1 Formulation

Following the generic formulation of a rate-independent, small-strain plasticity model described in Section 3.1, in an incremental strain-controlled algorithm, for a given strain increment $\Delta\boldsymbol{\epsilon}$, the standard procedure is to first assume that the material response is elastic. The trial stress is then calculated as $\boldsymbol{\sigma}^{\text{tr}} := \boldsymbol{\sigma}(\boldsymbol{\epsilon}, {}^{n}\mathbb{S})$. The elastic assumption holds if $\Phi^{\text{tr}} := \Phi(\boldsymbol{\sigma}^{\text{tr}}, {}^{n}\mathbb{A}) < 0$, thereby $\boldsymbol{\sigma} = \boldsymbol{\sigma}^{\text{tr}}$ and $\mathbb{S} = {}^{n}\mathbb{S}$. Otherwise, the set of DAEs, i.e, $\phi = 0$ and $\dot{\mathfrak{s}}_i = \dot{\lambda}\, \mathfrak{f}_i\left(\boldsymbol{\sigma}(\boldsymbol{\epsilon}, \mathbb{S}),\ \mathbb{A}(\boldsymbol{\epsilon}, \mathbb{S})\right)$ (Equation 3.3), must be solved.

Implicit or explicit time integration schemes, $\mathfrak{g}_i^{\text{TI}}$, can be used to approximate the solution to the evolution equations of the state variables in Equation 3.3

$$\Delta\mathfrak{s}_i = \mathfrak{g}_i^{\text{TI}}({}^{n}\boldsymbol{\epsilon},\ \Delta\boldsymbol{\epsilon},\ {}^{n}\mathbb{S}) \tag{7.4}$$

In implicit algorithms, $\mathfrak{g}_i^{\text{TI}}$ generally requires solving a nonlinear system of equations iteratively [145]. In explicit algorithms, when the material response transitions from elastic to plastic behavior, the intersection between the trial stress path and the yield surface is first determined in order to calculate the plastic part of the prescribed strain increment [146]. This introduces the elastic limit stress, $\boldsymbol{\sigma}^{\text{lim}}$, as

$$\boldsymbol{\sigma}^{\text{lim}} = \boldsymbol{\sigma}\left({}^{n}\boldsymbol{\epsilon} + s\,\Delta\boldsymbol{\epsilon}, {}^{n}\mathbb{S}\right) \tag{7.5}$$

where the scalar variable $s \in [0, 1]$ is determined from $\Phi(\boldsymbol{\sigma}^{\text{lim}}, {}^{n}\mathbb{A}) = 0$. Since $\Phi < 0$ during this elastic substep, no evolution of the state variables occurs. $\mathfrak{g}_i^{\text{TI}}$ therefore acts only on the plastic part of the strain increment as

$$\Delta\mathfrak{s}_i = \mathfrak{g}_i^{\text{TI}}({}^{n}\boldsymbol{\epsilon} + s\Delta\boldsymbol{\epsilon},\ [1-s]\Delta\boldsymbol{\epsilon},\ {}^{n}\mathbb{S}) \tag{7.6}$$

$\Phi = 0$ and Equation 3.3 are the DAEs to be solved to calculate $\Delta\mathfrak{s}_i$. In explicit integration schemes, the solution for the increment of the plastic multiplier, $\Delta\lambda$, can typically be obtained analytically from the consistency condition $\Phi(\boldsymbol{\sigma}, \mathbb{A}) = 0$. Explicit time integration can therefore be computationally efficient compared to the implicit time integration schemes, but small time increments are required to ensure numerical stability.

In **Paper D**, an explicit NN-based time integrator, $\mathfrak{g}_{\mathfrak{s}_i}^{\text{NN}}$, was introduced for the evolution of the state variables. The objective was to allow very large strain increments to reduce the computational cost of solving the DAEs without compromising accuracy and numerical stability. The formulation of $\mathfrak{g}_{\mathfrak{s}_i}^{\text{NN}}$ is

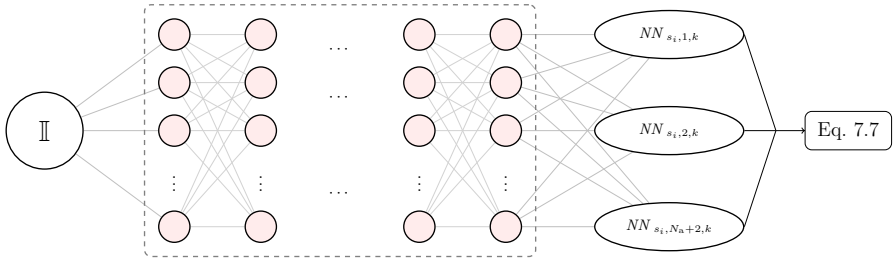


Figure 7.4: Schematic illustration of the inputs and outputs of the FFNN embedded in Equation 7.7.

given by

$$\mathfrak{g}_{\mathfrak{s}_i}^{\mathrm{NN}}({}^n\boldsymbol{\epsilon} + s\Delta\boldsymbol{\epsilon},\ [1-s]\Delta\boldsymbol{\epsilon},\ {}^n\mathbb{S}) = \sum_{k=1}^{N}\left[\mathcal{NN}_{\mathfrak{s}_i,\,1,\,k}(\mathbb{I})\frac{\partial I_k}{\partial \boldsymbol{\sigma}^{\mathrm{tr}}} + \mathcal{NN}_{\mathfrak{s}_i,\,2,\,k}(\mathbb{I})\frac{\partial I_k}{\partial \boldsymbol{\sigma}^{\mathrm{lim}}} + \sum_{j=1}^{N_{\mathrm{a}}}\mathcal{NN}_{\mathfrak{s}_i,\,j+2,\,k}(\mathbb{I})\frac{\partial I_k}{\partial {}^n\mathfrak{a}_j}\right] \tag{7.7}$$

where $\mathcal{NN}$ are scalar outputs of a FFNN; see Figure 7.4. $\mathbb{I} = \{I_1,\ I_2,\ \cdots,\ I_N\}$ is a set of suitable invariants of $\boldsymbol{\sigma}^{\mathrm{tr}}$, $\boldsymbol{\sigma}^{\mathrm{lim}}$, and ${}^n\mathfrak{a}_j$. The derivatives of these invariants with respect to $\boldsymbol{\sigma}^{\mathrm{tr}}$, $\boldsymbol{\sigma}^{\mathrm{lim}}$, and ${}^n\mathfrak{a}_j$ define the evolution directions of the state variables. The consistency condition during plastic loading, i.e., $\Phi(\boldsymbol{\sigma}, \mathbb{A}) = 0$, is inherently fulfilled through the correction factor c, which gives the increments of the state variables as $\Delta\mathfrak{s}_i = c\,\mathfrak{g}_{\mathfrak{s}_i}^{\mathrm{NN}}$. In **Paper D**, it was chosen to express the NNs in terms of invariants to satisfy the frame-invariance condition by construction. This approach is computationally more efficient than training the NNs on many transformed versions of data to learn the invariance property [147]. Furthermore, this choice improved the generalization performance of the NN-based time integrator. In particular, it was trained on only 10 cycles of 2D multiaxial proportional cyclic loading but achieved excellent predictions on 100 cycles of 3D loading.

The proposed framework in **Paper D** is physics-encoded, since essential plasticity constraints, i.e., objectivity, consistency condition, and the distinction between elastic and plastic response, are satisfied by construction.

7.3.2 Numerical performance evaluation

In **Paper D**, the NN-based time integrator was applied to solve the DAEs of two prototype material models based on the von Mises yield function: one employing the simple AF kinematic hardening law and the other employing the more nonlinear OW hardening law, as described in Chapter 3. After training, the numerical performance of the NN-based time integrator was examined through both material point and FE simulations in terms of accuracy and computational efficiency. As an example, Figure 7.5 shows the deviatoric axial

and shear stress-strain responses of the OW-based prototype model under 3D deviatoric multiaxial pulsating loading. In this figure, the reference solution (shown by blue lines) was obtained by integrating the OW-based prototype model with the implicit backward Euler time integration algorithm. Each cycle was discretized with very small time steps, i.e., 400 time steps per cycle, such that the reference solution can be regarded as the true solution. The predictions obtained with the NN-based time integrator using 5 and 1 increments per load segment show close agreement with this reference solution. Despite being an explicit scheme and being trained only on 10 cycles of 2D loading, the NN-based time integrator showed very good performance for large strain increments and generalized well to 3D loading over 100 cycles.

7.3.3 Application to wheel over-rolling simulations

After successful evaluation of the proposed time integrator in FE simulations of an academic example in **Paper D**, it is incorporated here into wheel over-rolling FE simulations. The assumed loading conditions and geometry are the same as those in **Paper B**. The von Mises stress, σ^{vM}, distributions in railheads with initial material and deformed geometry in the last over-rolling cycle are illustrated in Figure 7.6. For both railheads, the prototype material model from **Paper D**, based on the von Mises yield function and the AF kinematic hardening law, is employed, while the time-integration schemes differ. The reference FE solution employs the backward Euler time integrator with 25 load increments per load segment, and the FE model with the NN-based time integrator uses 5 increments per load segment. As can be seen in Figure 7.6, the results obtained with the NN-based time integrator are in close agreement with the reference solutions. Moreover, the maximum absolute error in σ^{vM}, considering all finite elements and all 382 simulated cycles, is less than 1.5% of the maximum reference value of 886 MPa. It is important to note that the simulation using the NN-based integrator was approximately four times faster than the simulation with the backward Euler time integrator.

These results demonstrate the potential of applying the NN-based time integrator to complex FE simulations, such as rolling contact simulations involving many wheel passages.

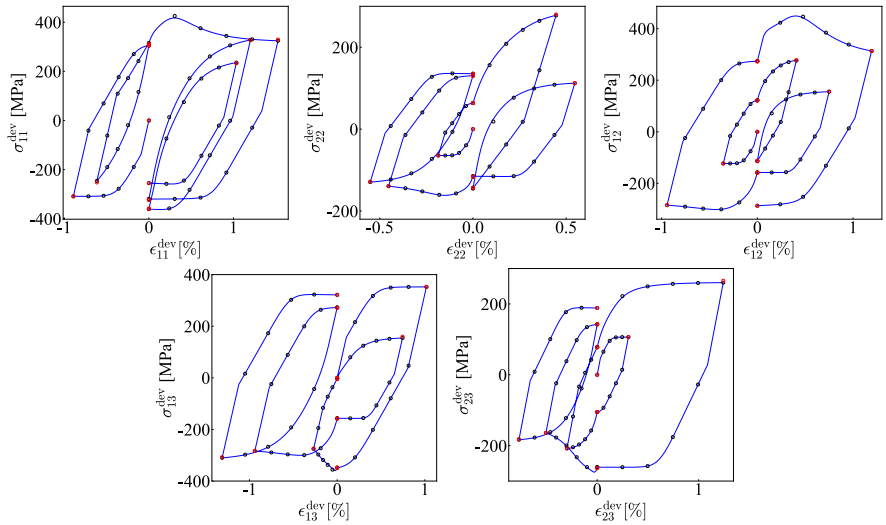


Figure 7.5: The first 5 stress-strain cycles from the 3D test data generated with the OW-based material model (blue) compared with predictions obtained with the NN-based time integration scheme, from **Paper D**. The black and red circles correspond to the NN-based predictions using 5 and 1 strain increments per half-cycle, respectively.

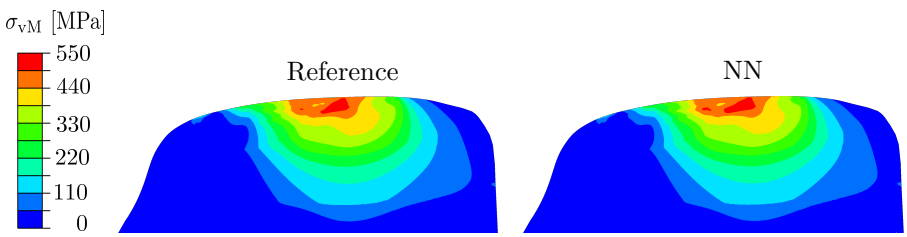


Figure 7.6: von Mises stress distributions in the railheads subjected to wheel-rail contact loading. NN refers to the NN-based time integration (developed in **Paper D**) of the FE model.

CHAPTER 8

Concluding remarks and outlook

8.1 Concluding remarks

The aim of this thesis was to advance the accuracy and computational efficiency of numerical tools for predicting RCF crack initiation in highly deformed rail steel. The research objectives outlined in Section 1.2 were pursued in **Papers A–D**, as summarized below.

Objective 1: Determine a suitable fatigue crack initiation criterion that takes into account the effect of the highly deformed material in the surface layer of rails.

This research objective was investigated in **Paper A**. The study started from an evaluation of commonly used fatigue crack initiation criteria in railway engineering for predicting experimental results of highly deformed R260 pearlitic steel and proposed modifications to improve their performance. The assessment was based on combined axial-torsion tests with large shear strain increments (predeformation), proportional multiaxial LCF experiments preceded by different levels of predeformation, and uniaxial HCF tests. FE simulations of the predeformation tests, using a finite-strain plasticity model accounting for isotropic, kinematic, and distortional hardening, provided the local stress and strain predictions. A cross-validation approach was adopted to assess the criteria. One of the proposed modifications noticeably reduced the fitting error while maintaining a similar prediction error. It was also able to fit satisfactorily when all experimental data were included in the calibration, indicating its potential for further improvements with the availability of more experimental data.

Objective 2: Develop a framework to investigate the impact of the highly deformed near-surface material and deformed rail profile geometry on RCF crack initiation predictions.

As part of the framework developed in **Paper B**, an anisotropic plasticity model was calibrated against multiaxial LCF experiments under non-proportional loading at different levels of predeformation, representing the material behavior for different amounts of accumulated shear strain. By doing so, a model that

represents material behavior at different spatial positions in the railhead cross-section was obtained. This variation was governed by the accumulated shear strain distribution in the railhead, reconstructed from measured shear strains in field samples. A 2D generalized plane strain FE simulation setup was used for modeling four distinct railheads subjected to mixed traffic situations: (1) initial geometry with initial material, (2) initial geometry with inhomogeneously deformed (anisotropic) material, (3) deformed geometry with initial material, and (4) deformed geometry with deformed material. The results demonstrated that the deformed and hardened material leads to much higher maximum von Mises stresses but lower per-sequence accumulated plasticity than the initial material. Deformed railhead geometry reduced the frequency of load cases causing high von Mises stresses and accumulated plasticity. Using the crack initiation criterion proposed in **Paper A**, the fatigue damage per load sequence was evaluated. Both deformed material and geometry lowered the maximum accumulated damage, with the influence of the deformed geometry being more pronounced. Neglecting their combined effect led to about 150 times larger predictions of RCF damage.

Objective 3: Develop computationally efficient ML-based approaches for simulating cyclic plasticity.

The third objective of this thesis was explored in **Papers C** and **D**. The idea in **Paper C** was to replace a conventional time-domain model with a cycle-domain model, which predicts the peak stress and corresponding plastic strain in each cycle. Since formulating suitable per-cycle evolution laws for state variables, such as plastic strain, is challenging in such models, ML methods were investigated for describing the plastic strain evolution using either FFNNs or SR with different input features. Training, validation, and test data were generated using a standard time-domain plasticity model under pulsating uniaxial stress loading with constant and variable strain ranges. The study showed that both the NN- and SR-based cycle-domain models can reproduce the cyclic response with high accuracy. Although SR achieved human-readable evolution laws, there is a trade-off between interpretability and accuracy. Furthermore, both ML-based models showed very good performance when applied to 5000 loading cycles, more than 50 times longer than the number of cycles in the training.

In **Paper D**, a different strategy was investigated regarding the third objective. The time-domain formulation was retained, and, for the increment of state variables, NNs were used to formulate an explicit time integrator that can handle very large strain increments while preserving accuracy and numerical stability. The NNs operated on invariants, and the necessary and sufficient evolution directions were inferred from the training data. Moreover, the framework exactly satisfied the plastic consistency condition during plastic loading. The approach was evaluated using two prototype material models, both based on the von Mises yield criterion but with different nonlinear kinematic hardening laws. The results from material point simulations showed that the proposed NN-based time integrator provides accurate and numerically robust predictions, even when using a single strain increment per half-cycle.

Despite being trained only on 2D loading over 10 cycles, it generalized well to 3D loading over 100 cycles. In the FE simulations, the maximum error in the von Mises stresses remained below 2% of the maximum stress over 100 cycles. At comparable accuracy, the NN-based time integration of the FE model with a single increment per load segment was about 3 times faster than the conventional backward Euler integration scheme.

In the next step, the numerical framework in **Paper D** was embedded in wheel over-rolling simulations considering a geometrically deformed railhead with initial material state, subjected to the same loading conditions as those in **Paper B**. The maximum absolute error in the von Mises stress, considering the whole rail domain and all simulated cycles, was less than 1.5%. In addition, the simulation using the NN-based time integrator was about 4 times faster than the simulations using the backward Euler scheme.

8.2 Outlook

This thesis opens up several interesting directions for future research, some of which are presented in this section. The NN-based time-integration framework developed in **Paper D** and successfully tested for FE simulations of wheel over-rollings in Section 7.3.3 should be embedded within the framework of **Paper B**. In particular, the plasticity model in **Paper B** with an anisotropic yield surface should be used for training of the NN-based time integrator. More challenging loading paths, including non-proportional multiaxial loadings, can be used for training data generation to improve its applicability to wheel-rail contact conditions. Based on the computational gains demonstrated in **Paper D** and in this thesis, such an implementation could enable simulations involving much larger numbers of wheel over-rollings, and thereby move towards more realistic predictions of RCF crack initiation.

Further reductions in computational cost can be achieved by combining the NN-based time integrator with reduced-order modeling approaches, as shown in [19]. Such an approach would be particularly attractive for long-term forecasts of damage evolution in rails, where material properties and rail profile geometry evolve during the loading sequences. In this case, incorporating more detailed tribological mechanisms and their interaction, including wear, plastic deformation, and RCF crack initiation, is necessary.

Another direction for future work is to use the stress, strain, and fatigue-damage fields obtained from the numerical framework developed in **Paper B** as initial conditions for subsequent crack-propagation analyses. This would enable investigation of how the highly deformed and anisotropic near-surface material influences the growth of surface-initiated RCF cracks.

Bibliography

[1] A. Ekberg, B. Åkesson and E. Kabo, 'Wheel/rail rolling contact fatigue – probe, predict, prevent,' *Wear*, vol. 314, pp. 2–12, 2014.

[2] Trafikverket, 'Trafikverkets årsredovisning 2024,' Trafikverket, Borlänge, Sweden, Technical Report (In Swedish), 2025:006, 2025.

[3] E. E. Magel, 'Rolling contact fatigue: A comprehensive review,' US Department of Transportation, Federal Railroad Administration, Technical Report, 132 p., 2011.

[4] A. Kapoor, I. Salehi and A. M. S. Asih, 'Rolling contact fatigue (rcf),' in *Encyclopedia of Tribology*, Q. J. Wang and Y.-W. Chung, Eds. Boston, MA: Springer US, 2013, pp. 2904–2910.

[5] F. Dörner, C. Körblein and C. Schindler, 'On the accuracy of the pressure measurement film in hertzian contact situations similar to wheel-rail contact applications,' *Wear*, vol. 317, no. 1-2, pp. 241–245, 2014.

[6] K. Johnson, 'The strength of surfaces in rolling contact,' *Proceedings of the Institution of Mechanical Engineers, Part C: Journal of Mechanical Engineering Science*, vol. 203, no. 3, pp. 151–163, 1989.

[7] F. A. Alwahdi, A. Kapoor and F. J. Franklin, 'Subsurface microstructural analysis and mechanical properties of pearlitic rail steels in service,' *Wear*, vol. 302, pp. 1453–1460, 2013.

[8] B. Dylewski, M. Risbet and S. Bouvier, 'The tridimensional gradient of microstructure in worn rails – Experimental characterization of plastic deformation accumulated by RCF,' *Wear*, vol. 392-393, pp. 50–59, 2017.

[9] D. F. Cannon, K. Edel, S. L. Grassie and K. Sawley, 'Rail defects: An overview,' *Fatigue and Fracture of Engineering Materials and Structures*, vol. 26, pp. 865–886, 2003.

[10] R. Smallwood, J. Sinclair and K. Sawley, 'An optimization technique to minimize rail contact stresses,' *Wear*, vol. 144, no. 1-2, pp. 373–384, 1991.

[11] N. Mahdavinasab, Z. Beg, J. Barabady, U. Juntti and A. Garmabaki, 'The effect of climate condition on the CO_2 emissions of maintenance activities: A case study from railway,' *Proceedings of the 35th European Safety and Reliability & the 33rd Society for Risk Analysis Europe Conference*, 2025.

[12] K. A. Meyer, D. Nikas and J. Ahlström, 'Microstructure and mechanical properties of the running band in a pearlitic rail steel: Comparison between biaxially deformed steel and field samples,' *Wear*, vol. 396-397, pp. 12–21, 2018.

[13] J. Garnham and C. Davis, 'Very early stage rolling contact fatigue crack growth in pearlitic rail steels,' *Wear*, vol. 271, no. 1-2, pp. 100–112, 2011.

[14] F. Wetscher, R. Stock and R. Pippan, 'Changes in the mechanical properties of a pearlitic steel due to large shear deformation,' *Materials Science and Engineering A*, vol. 445-446, pp. 237–243, 2007.

[15] T. Leitner, A. Hohenwarter and R. Pippan, 'Anisotropy in fracture and fatigue resistance of pearlitic steels and its effect on the crack path,' *International Journal of Fatigue*, vol. 124, pp. 528–536, 2019.

[16] J. N. Fuhg et al., 'A review on data-driven constitutive laws for solids,' *Archives of Computational Methods in Engineering*, pp. 1–43, 2024.

[17] S. Rezaei, A. Moeineddin and A. Harandi, 'Learning solutions of thermodynamics-based nonlinear constitutive material models using physics-informed neural networks,' *Computational Mechanics*, vol. 74, no. 2, pp. 333–366, 2024.

[18] P. Zhang, 'Neural network based numerical integration for elastoplastic constitutive relations,' *Computers and Geotechnics*, vol. 190, p. 107 721, 2026.

[19] P. E. Malleval, V. Matray, F. Amlani and R. Scanff, 'Accelerating nonlinear finite element analysis via residual-aware neural network constitutive models,' *Finite Elements in Analysis & Design*, vol. 251, no. July, p. 104 431, 2025.

[20] P. Pointner, A. Joerg and J. Jaiswal, 'Definitive guidelines on the use of different rail grades,' *INNOTRACK GUIDELINE*, pp. 1–45, 2006.

[21] SIS, 'Railway applications – Track – Rail – Part 1: Vignole railway rails 46 kg/m and above,' Swedish Institute for Standards (SIS), SS-EN 13674-1:2011+A1:2017, 2017.

[22] K. A. Meyer, 'Modeling and experimental characterization of large biaxial strains and induced anisotropy in pearlitic rail steel,' PhD thesis, Chalmers University of Technology (Sweden), 2019.

[23] N. Larijani, J. Brouzoulis, M. Schilke and M. Ekh, 'The effect of anisotropy on crack propagation in pearlitic rail steel,' *Wear*, vol. 314, no. 1-2, pp. 57–68, 2014.

[24] H. Eden, J. Garnham and C. Davis, 'Influential microstructural changes on rolling contact fatigue crack initiation in pearlitic rail steels,' *Materials science and technology*, vol. 21, no. 6, pp. 623–629, 2005.

[25] A. Hohenwarter, A. Taylor, R. Stock and R. Pippan, 'Effect of large shear deformations on the fracture behavior of a fully pearlitic steel,' *Metallurgical and Materials Transactions A: Physical Metallurgy and Materials Science*, vol. 42, pp. 1609–1618, 2011.

[26] K. A. Meyer, M. Ekh and J. Ahlström, 'Anisotropic yield surfaces after large shear deformations in pearlitic steel,' *European Journal of Mechanics, A/Solids*, vol. 82, p. 103 977, 2020.

[27] T. Leitner, G. Trummer, R. Pippan and A. Hohenwarter, 'Influence of severe plastic deformation and specimen orientation on the fatigue crack propagation behavior of a pearlitic steel,' *Materials Science and Engineering: A*, vol. 710, pp. 260–270, 2018.

[28] D. Gren and J. Ahlström, 'Fatigue crack propagation on uniaxial loading of biaxially predeformed pearlitic rail steel,' *Metals*, vol. 13, p. 1726, 2023.

[29] E. Magel, P. Mutton, A. Ekberg and A. Kapoor, 'Rolling contact fatigue, wear and broken rail derailments,' *Wear*, vol. 366, pp. 249–257, 2016.

[30] D. I. Fletcher, F. J. Franklin and A. Kapoor, 'Rail surface fatigue and wear,' in *Wheel–rail interface handbook,* Elsevier, pp. 280–310, 2009.

[31] S. Iwnicki, *Handbook of railway vehicle dynamics*. CRC press, 2006.

[32] N. P. Suh, 'An overview of the delamination theory of wear,' *Wear*, vol. 44, no. 1, pp. 1–16, 1977.

[33] G. Trummer, C. Marte, P. Dietmaier, C. Sommitsch and K. Six, 'Modeling surface rolling contact fatigue crack initiation taking severe plastic shear deformation into account,' *Wear*, vol. 352, pp. 136–145, 2016.

[34] J. Lemaitre, *A course on damage mechanics*. Springer science & business media, 2012.

[35] F. Sadeghi, B. Jalalahmadi, T. S. Slack, N. Raje and N. K. Arakere, 'A review of rolling contact fatigue,' *Journal of Tribology*, vol. 131, pp. 1–15, 2009.

[36] J. W. Ringsberg, 'Life prediction of rolling contact fatigue crack initiation,' *International Journal of Fatigue*, vol. 23, pp. 575–586, 2001.

[37] A. Kapoor, 'A re-evaluation of the life to rupture of ductile metals by cyclic plastic strain,' *Fatigue & Fracture of Engineering Materials & Structures*, vol. 17, pp. 201–219, 1994.

[38] K. Golos and F. Ellyin, 'A total strain energy density theory for cumulative fatigue damage,' *Journal of Pressure Vessel Technology, Transactions of the ASME*, vol. 110, pp. 36–41, 1988.

[39] F. J. Franklin, J. E. Garnham, D. I. Fletcher, C. L. Davis and A. Kapoor, 'Modelling rail steel microstructure and its effect on crack initiation,' *Wear*, vol. 265, pp. 1332–1341, 2008.

[40] M. D. Sangid, H. J. Maier and H. Sehitoglu, 'The role of grain boundaries on fatigue crack initiation–an energy approach,' *International Journal of Plasticity*, vol. 27, no. 5, pp. 801–821, 2011.

[41] M. Ghodrati, M. Ahmadian and R. Mirzaeifar, 'Modeling of rolling contact fatigue in rails at the microstructural level,' *Wear*, vol. 406-407, pp. 205–217, 2018.

[42] M. W. Brown and K. J. Miller, 'A theory for fatigue failure under multiaxial stress-strain conditions,' *Proceedings of the Institution of Mechanical Engineers*, vol. 187, pp. 745–755, 1973.

[43] K. N. Smith, T. H. Topper and P. Watson, 'A stress-strain function for the fatigue of metals (stress-strain function for metal fatigue including mean stress effect),' *Journal of Materials*, vol. 5, pp. 767–778, 1970.

[44] A. Ince and G. Glinka, 'A generalized fatigue damage parameter for multiaxial fatigue life prediction under proportional and non-proportional loadings,' *International Journal of Fatigue*, vol. 62, pp. 34–41, 2014.

[45] C. L. Pun, Q. Kan, P. J. Mutton, G. Kang and W. Yan, 'A single parameter to evaluate stress state in rail head for rolling contact fatigue analysis,' *Fatigue and Fracture of Engineering Materials and Structures*, vol. 37, pp. 909–919, 2014.

[46] S. Döbrentei and P. T. Zwierczyk, 'A proposal for a novel energy-based critical plane parameter, including equivalent plastic strain, stress triaxility and material ductility,' *Results in Engineering*, p. 111 376, 2026.

[47] Y. Jiang and H. Sehitoglu, 'A model for rolling contact failure,' *Wear*, vol. 224, pp. 38–49, 1999.

[48] D. Benoît, B. Salima and R. Marion, 'Multiscale characterization of head check initiation on rails under rolling contact fatigue: Mechanical and microstructure analysis,' *Wear*, vol. 366-367, pp. 383–391, 2016.

[49] K. A. Meyer and A. Menzel, 'A distortional hardening model for finite plasticity,' *International Journal of Solids and Structures*, vol. 232, p. 111 055, 2021.

[50] E. Lindfeldt and M. Ekh, 'On the prediction of macroscopic yield surfaces for a pearlitic steel using computational homogenization,' *Journal of Multiscale Modelling*, vol. 04, no. 02, p. 1 250 006, 2012.

[51] A. Vijay and F. Sadeghi, 'A continuum damage mechanics framework for modeling the effect of crystalline anisotropy on rolling contact fatigue,' *Tribology International*, vol. 140, p. 105 845, 2019.

[52] R. Skrypnyk, J. Ekh Magnus and B. A. Pålsson, 'Prediction of plastic deformation and wear in railway crossings–comparing the performance of two rail steel grades,' *Wear*, vol. 428, pp. 302–314, 2019.

[53] K. A. Meyer, R. Skrypnyk and M. Pletz, 'Efficient 3d finite element modeling of cyclic elasto-plastic rolling contact,' *Tribology International*, vol. 161, p. 107 053, 2021.

[54] K. Pack, T. Tancogne-Dejean, M. B. Gorji and D. Mohr, 'Hosford-coulomb ductile failure model for shell elements: Experimental identification and validation for DP980 steel and aluminum 6016-T4,' *International Journal of Solids and Structures*, vol. 151, pp. 214–232, 2018.

[55] J. Ghaboussi, D. A. Pecknold and X. S. Wu, *Nonlinear computational solid mechanics*. CRC Press, 2017.

[56] M. Ekh, A. Johansson, H. Thorberntsson and B. L. Josefson, 'Models for cyclic ratchetting plasticity—integration and calibration,' *Journal of Engineering Materials and Technology*, vol. 122, pp. 49–55, 2000.

[57] C. Frederick and P. Armstrong, 'A mathematical representation of the multiaxial bauschinger effect,' *Materials at High Temperatures*, vol. 24, no. 1, pp. 1–26, 2007.

[58] H. P. Feigenbaum and Y. F. Dafalias, 'Directional distortional hardening in metal plasticity within thermodynamics,' *International Journal of Solids and Structures*, vol. 44, no. 22, pp. 7526–7542, 2007.

[59] M. P. Pietryga, I. N. Vladimirov and S. Reese, 'A finite deformation model for evolving flow anisotropy with distortional hardening including experimental validation,' *Mechanics of Materials*, vol. 44, pp. 163–173, 2012.

[60] B. Shi, A. Bartels and J. Mosler, 'On the thermodynamically consistent modeling of distortional hardening: A novel generalized framework,' *International Journal of Plasticity*, vol. 63, pp. 170–182, 2014.

[61] R. Hill, 'A theory of the yielding and plastic flow of anisotropic metals,' *Proceedings of the Royal Society of London. A. Mathematical and Physical Sciences*, vol. 193, no. 1033, pp. 281–297, 1948.

[62] D. Banabic, T. Kuwabara, T. Balan, D. Comsa and D. Julean, 'Non-quadratic yield criterion for orthotropic sheet metals under plane-stress conditions,' *International Journal of Mechanical Sciences*, vol. 45, no. 5, pp. 797–811, 2003.

[63] F. Barlat, H. Aretz, J. Yoon, M. Karabin, J. Brem and R. Dick, 'Linear transfomation-based anisotropic yield functions,' *International Journal of Plasticity*, vol. 21, no. 5, pp. 1009–1039, 2005.

[64] Z. He, K. Zhang, H. Zhu, Y. Lin, M. Fu and S. Yuan, 'An anisotropic constitutive model for forming of aluminum tubes under both biaxial tension and pure shear stress states,' *International Journal of Plasticity*, vol. 152, p. 103 259, 2022.

[65] W. Prager, 'A new method of analyzing stresses and strains in work-hardening plastic solids,' *Journal of Applied Mechanics*, vol. 23, no. 4, pp. 493–496, 1956.

[66] B. Andersson, J. Ahlström, M. Ekh and B. L. Josefson, 'Homogenization based macroscopic model of phase transformations and cyclic plasticity in pearlitic steel,' *Journal of Thermal Stresses*, vol. 45, no. 6, pp. 470–492, 2022.

[67] M. Subasic, A. Ireland, R. Mansour, P. Enblom, P. Krakhmalev and M. Åsberg, 'Experimental investigation and numerical modelling of the cyclic plasticity and fatigue behavior of additively manufactured 316 L stainless steel,' *International Journal of Plasticity*, vol. 176, no. April, p. 103 966, 2024.

[68] S. Bari and T. Hassan, 'An advancement in cyclic plasticity modeling for multiaxial ratcheting simulation,' *International Journal of Plasticity*, vol. 18, no. 7, pp. 873–894, 2002.

[69] M. Abdel-karim, 'An evaluation for several kinematic hardening rules on prediction of multiaxial stress-controlled ratchetting,' *International Journal of Plasticity*, vol. 26, no. 5, pp. 711–730, 2010.

[70] N. Ohno and J.-D. Wang, 'Kinematic hardening rules with critical state of dynamic recovery, part i: Formulation and basic features for ratchetting behavior,' *International Journal of Plasticity*, vol. 9, no. 3, pp. 375–390, 1993.

[71] R. Brommesson, M. Ekh and M. Hörnqvist, 'Correlation between crack length and load drop for low-cycle fatigue crack growth in Ti-6242,' *International Journal of Fatigue*, vol. 81, pp. 1–9, 2015.

[72] R. Skrypnyk, J. C. O. Nielsen, M. Ekh and B. A. Pålsson, 'Metamodelling of wheel–rail normal contact in railway crossings with elasto-plastic material behaviour,' *Engineering with Computers*, vol. 35, no. 1, pp. 139–155, 2019.

[73] T. Lindström, D. Ewest, K. Simonsson, R. Eriksson, J.-E. Lundgren and D. Leidermark, 'Constitutive model of an additively manufactured ductile nickel-based superalloy undergoing cyclic plasticity,' *International Journal of Plasticity*, vol. 132, p. 102 752, 2020.

[74] P. Delobelle, P. Robinet and L. Bocher, 'Experimental study and phenomenological modelization of ratchet under uniaxial and biaxial loading on an austenitic stainless steel,' *International Journal of Plasticity*, vol. 11, no. 4, pp. 295–330, 1995.

[75] H. Burlet and G. Cailletaud, 'Numerical techniques for cyclic plasticity at variable temperature,' *Engineering Computations*, vol. 3, no. 2, pp. 143–153, 1986.

[76] L. Reis, B. Li and M. de Freitas, 'A multiaxial fatigue approach to rolling contact fatigue in railways,' *International Journal of Fatigue*, vol. 67, pp. 191–202, 2014.

[77] C. L. Pun, Q. Kan, P. J. Mutton, G. Kang and W. Yan, 'Ratcheting behaviour of high strength rail steels under bi-axial compression-torsion loadings: Experiment and simulation,' *International Journal of Fatigue*, vol. 66, pp. 138–154, 2014.

[78] P. I. Christodoulou, A. T. Kermanidis and G. N. Haidemenopoulos, 'Fatigue and fracture behavior of pearlitic Grade 900A steel used in railway applications,' *Theoretical and Applied Fracture Mechanics*, vol. 83, pp. 51–59, 2016.

[79] J. A. Nelder and R. Mead, 'A simplex method for function minimization,' *The Computer Journal*, vol. 7, pp. 308–313, 1965.

[80] M. J. Powell, 'The BOBYQA algorithm for bound constrained optimization without derivatives,' *Cambridge NA Report NA2009/06, University of Cambridge, Cambridge*, vol. 26, pp. 26–46, 2009.

[81] N. Andréasson et al., *An Introduction to Continuous Optimization, 3rd edition. Studentlitteratur*, 2016.

[82] L. Liu et al., 'On the variance of the adaptive learning rate and beyond,' *arXiv:1908.03265*, 2019.

[83] K. A. Meyer, 'Evaluation of material models describing the evolution of plastic anisotropy in pearlitic steel,' *International Journal of Solids and Structures*, vol. 200, pp. 266–285, 2020.

[84] M. Stone, 'Cross-validatory choice and assessment of statistical predictions,' *Journal of the Royal Statistical Society*, vol. 36, pp. 111–147, 1974.

[85] D. Hérault, S. Thuillier, S. Y. Lee, P. Y. Manach and F. Barlat, 'Calibration of a strain path change model for a dual phase steel,' *International Journal of Mechanical Sciences*, vol. 194, 2021.

[86] Dassault Systèmes Simulia Corp., *Abaqus analysis user's manual*, 2022nd ed., Available from Dassault Systèmes, Providence, Rhode Island, USA, 2022.

[87] J. W. Ringsberg, 'Life prediction of rolling contact fatigue crack initiation,' *International Journal of Fatigue*, vol. 23, pp. 575–586, 2001.

[88] K. Vo, H. Zhu, A. K. Tieu and P. Kosasih, 'FE method to predict damage formation on curved track for various worn status of wheel/rail profiles,' *Wear*, vol. 322, pp. 61–75, 2015.

[89] M. Ghodrati, M. Ahmadian and R. Mirzaeifar, 'Three-dimensional study of rolling contact fatigue using crystal plasticity and cohesive zone method,' *International Journal of Fatigue*, vol. 128, p. 105 208, 2019.

[90] M. Pletz, K. A. Meyer, D. Künstner, S. Scheriau and W. Daves, 'Cyclic plastic deformation of rails in rolling/sliding contact –quasistatic FE calculations using different plasticity models,' *Wear*, vol. 436-437, p. 202 992, 2019.

[91] M. S. Nezhad, F. Larsson, E. Kabo and A. Ekberg, 'Finite element analyses of rail head cracks: Predicting direction and rate of rolling contact fatigue crack growth,' *Engineering Fracture Mechanics*, vol. 310, p. 110 503, 2024.

[92] Z. Zhou, W. Li, Z. Wen, S. Zhou and G. Tao, 'Three-dimensional elastic–plastic stress analysis of wheel–rail cyclic rolling contact using finite element method,' *Wear*, vol. 542-543, p. 205 277, 2024.

[93] F. Ren, Z. Yang and Z. Li, 'An efficient 3D finite element procedure for simulating wheel–rail cyclic contact and ratcheting,' *Tribology International*, vol. 198, p. 109 878, 2024.

[94] J. Brouzoulis and M. Ekh, 'Crack propagation in rails under rolling contact fatigue loading conditions based on material forces,' *International Journal of Fatigue*, vol. 45, pp. 98–105, 2012.

[95] W. Daves, W. Kubin, S. Scheriau and M. Pletz, 'A finite element model to simulate the physical mechanisms of wear and crack initiation in wheel/rail contact,' *Wear*, vol. 366-367, pp. 78–83, 2016.

[96] B. Andersson, M. Ekh and B. L. Josefson, 'Computationally efficient simulation methodology for railway repair welding: Cyclic plasticity, phase transformations and multi-phase homogenization,' *Journal of Thermal Stresses*, vol. 47, pp. 164–188, 2024.

[97] C. Ansin, B. A. Pålsson, M. Ekh, F. Larsson and R. Larsson, 'Simulation and field measurements of the long-term rail surface damage due to plasticity, wear and surface rolling contact fatigue cracks in a curve,' *CM 2022 - 12th International Conference on Contact Mechanics and Wear of Rail/Wheel Systems, Conference Proceedings*, pp. 591–601, 2022.

[98] M. Harmon, J. Santa, J. Jaramillo, A. Toro, A. Beagles and R. Lewis, 'Evaluation of the coefficient of friction of rail in the field and laboratory using several devices,' *Tribology-Materials, Surfaces & Interfaces*, vol. 14, no. 2, pp. 119–129, 2020.

[99] H. Su, C. L. Pun, P. Mutton, Q. Kan and W. Yan, 'Numerical study on the ratcheting performance of heavy haul rails in curved tracks,' *Wear*, vol. 436, p. 203 026, 2019.

[100] G. Johansson and M. Ekh, 'On the modeling of large ratcheting strains with large time increments,' *Engineering Computations*, vol. 24, no. 3, pp. 221–236, 2007.

[101] H. Kiewel, J. Aktaa and D. Munz, 'Application of an extrapolation method in thermocyclic failure analysis,' *Computer methods in applied mechanics and engineering*, vol. 182, no. 1-2, pp. 55–71, 2000.

[102] D. Cojocaru and A. M. Karlsson, 'A simple numerical method of cycle jumps for cyclically loaded structures,' *International Journal of fatigue*, vol. 28, no. 12, pp. 1677–1689, 2006.

[103] S. Burlon, H. Mroueh and J. Cao, ''Skipped cycles' method for studying cyclic loading and soil–structure interface,' *Computers and Geotechnics*, vol. 61, pp. 209–220, 2014.

[104] A. Abdul-Latif, D. Razafindramary and J. Rakotoarisoa, 'New hybrid cycle jump approach for predicting low-cycle fatigue behavior by a micromechanical model with the damage induced anisotropy concept,' *International Journal of Mechanical Sciences*, vol. 160, pp. 397–411, 2019.

[105] F. E. Bock, R. C. Aydin, C. J. Cyron, N. Huber, S. R. Kalidindi and B. Klusemann, 'A review of the application of machine learning and data mining approaches in continuum materials mechanics,' *Frontiers in Materials*, vol. 6, p. 110, 2019.

[106] J. Ghaboussi, J. Garrett Jr and X. Wu, 'Knowledge-based modeling of material behavior with neural networks,' *Journal of engineering mechanics*, vol. 117, no. 1, pp. 132–153, 1991.

[107] Y. M. Hashash, S. Jung and J. Ghaboussi, 'Numerical implementation of a neural network based material model in finite element analysis,' *International Journal for numerical methods in engineering*, vol. 59, no. 7, pp. 989–1005, 2004.

[108] U. Ali, W. Muhammad, A. Brahme, O. Skiba and K. Inal, 'Application of artificial neural networks in micromechanics for polycrystalline metals,' *International Journal of Plasticity*, vol. 120, pp. 205–219, 2019.

[109] D. Huang, J. N. Fuhg, C. Weißenfels and P. Wriggers, 'A machine learning based plasticity model using proper orthogonal decomposition,' *Computer Methods in Applied Mechanics and Engineering*, vol. 365, p. 113 008, 2020.

[110] M. B. Gorji, M. Mozaffar, J. N. Heidenreich, J. Cao and D. Mohr, 'On the potential of recurrent neural networks for modeling path dependent plasticity,' *Journal of the Mechanics and Physics of Solids*, vol. 143, p. 103 972, 2020.

[111] R. Lourenço, A. Tariq, P. Georgieva, A. Andrade-Campos and B. Deliktaş, 'On the use of physics-based constraints and validation kpi for data-driven elastoplastic constitutive modelling,' *Computer Methods in Applied Mechanics and Engineering*, vol. 437, p. 117 743, 2025.

[112] M. Rosenkranz, K. A. Kalina, J. Brummund and M. Kästner, 'A comparative study on different neural network architectures to model inelasticity,' *International Journal for Numerical Methods in Engineering*, vol. 124, no. 21, pp. 4802–4840, 2023.

[113] M. Raissi, P. Perdikaris and G. E. Karniadakis, 'Physics-informed neural networks: A deep learning framework for solving forward and inverse problems involving nonlinear partial differential equations,' *Journal of Computational physics*, vol. 378, pp. 686–707, 2019.

[114] E. Haghighat, S. Abouali and R. Vaziri, 'Constitutive model characterization and discovery using physics-informed deep learning,' *Engineering Applications of Artificial Intelligence*, vol. 120, p. 105 828, 2023.

[115] P. Weber, W. Wagner and S. Freitag, 'Physically enhanced training for modeling rate-independent plasticity with feedforward neural networks,' *Computational Mechanics*, vol. 72, no. 4, pp. 827–857, 2023.

[116] P. Weber, J. Geiger and W. Wagner, 'Constrained neural network training and its application to hyperelastic material modeling,' *Computational Mechanics*, vol. 68, no. 5, pp. 1179–1204, 2021.

[117] K. A. Meyer and F. Ekre, 'Thermodynamically consistent neural network plasticity modeling and discovery of evolution laws,' *Journal of the Mechanics and Physics of Solids*, vol. 180, p. 105 416, 2023.

[118] J. N. Fuhg, C. M. Hamel, K. Johnson, R. Jones and N. Bouklas, 'Modular machine learning-based elastoplasticity: Generalization in the context of limited data,' *Computer Methods in Applied Mechanics and Engineering*, vol. 407, p. 115 930, 2023.

[119] A. A. Jadoon, K. A. Meyer and J. N. Fuhg, 'Automated model discovery of finite strain elastoplasticity from uniaxial experiments,' *Computer Methods in Applied Mechanics and Engineering*, vol. 435, p. 117 653, 2025.

[120] M. Flaschel, S. Kumar and L. De Lorenzis, 'Unsupervised discovery of interpretable hyperelastic constitutive laws,' *Computer Methods in Applied Mechanics and Engineering*, vol. 381, p. 113 852, 2021.

[121] M. Flaschel, S. Kumar and L. De Lorenzis, 'Automated discovery of generalized standard material models with euclid,' *Computer Methods in Applied Mechanics and Engineering*, vol. 405, p. 115 867, 2023.

[122] J. N. Fuhg, R. E. Jones and N. Bouklas, 'Extreme sparsification of physics-augmented neural networks for interpretable model discovery in mechanics,' *Computer Methods in Applied Mechanics and Engineering*, vol. 426, p. 116 973, 2024.

[123] Y. Wang, N. Wagner and J. M. Rondinelli, 'Symbolic regression in materials science,' *MRS communications*, vol. 9, no. 3, pp. 793–805, 2019.

[124] D. Versino, A. Tonda and C. A. Bronkhorst, 'Data driven modeling of plastic deformation,' *Computer Methods in Applied Mechanics and Engineering*, vol. 318, pp. 981–1004, 2017.

[125] G. Bomarito, T. Townsend, K. Stewart, K. Esham, J. Emery and J. Hochhalter, 'Development of interpretable, data-driven plasticity models with symbolic regression,' *Computers & Structures*, vol. 252, p. 106 557, 2021.

[126] R. Abdusalamov, M. Hillgärtner and M. Itskov, 'Automatic generation of interpretable hyperelastic material models by symbolic regression,' *International Journal for Numerical Methods in Engineering*, vol. 124, no. 9, pp. 2093–2104, 2023.

[127] F. Foroughi Boroujeni, A. Faramarzi, W. Cha and B. Ghiassi, 'A physics-informed evolutionary regression framework for constitutive modelling of sand,' *Computers and Geotechnics*, vol. 197, p. 108 179, 2026.

[128] K. Garbrecht, D. Birky, B. Lester, J. Emery and J. Hochhalter, 'Complementing a continuum thermodynamic approach to constitutive modeling with symbolic regression,' *Journal of the Mechanics and Physics of Solids*, vol. 181, p. 105 472, 2023.

[129] M. H. Ulz, 'Discovering symbolic solutions for mechanical problems using symbolic regression and parametric regression,' *Computers & Structures*, p. 108 466, 2026.

[130] K. P. Abdolazizi, R. C. Aydin, C. J. Cyron and K. Linka, 'Constitutive kolmogorov–arnold networks (CKANs): Combining accuracy and interpretability in data-driven material modeling,' *Journal of the Mechanics and Physics of Solids*, vol. 203, p. 106 212, 2025.

[131] A. Zhang and D. Mohr, 'Using neural networks to represent von mises plasticity with isotropic hardening,' *International Journal of Plasticity*, vol. 132, p. 102 732, 2020.

[132] D. P. Jang, P. Fazily and J. W. Yoon, 'Machine learning-based constitutive model for j2-plasticity,' *International Journal of Plasticity*, vol. 138, p. 102 919, 2021.

[133] P. Fazily and J. W. Yoon, 'Machine learning-driven stress integration method for anisotropic plasticity in sheet metal forming,' *International Journal of Plasticity*, vol. 166, p. 103 642, 2023.

[134] W. G. Dettmer, E. J. Muttio, R. Alhayki and D. Perić, 'A framework for neural network based constitutive modelling of inelastic materials,' *Computer Methods in Applied Mechanics and Engineering*, vol. 420, p. 116 672, 2024.

[135] M. Eghbalian, M. Pouragha and R. Wan, 'A physics-informed deep neural network for surrogate modeling in classical elasto-plasticity,' *Computers and Geotechnics*, vol. 159, no. April, 2023.

[136] Y. Li, J. M. Zhang and R. Wang, 'A pinn-driven stress integration paradigm for high-fidelity soil constitutive model considering cyclic response,' *Computers and Geotechnics*, vol. 196, p. 108 170, 2026.

[137] A. S. Suiker and R. de Borst, 'A numerical model for the cyclic deterioration of railway tracks,' *International Journal for Numerical Methods in Engineering*, vol. 57, no. 4, pp. 441–470, 2003.

[138] X. Li, M. Ekh and J. C. O. Nielsen, 'Three-dimensional modelling of differential railway track settlement using a cycle domain constitutive model,' *International Journal for Numerical and Analytical Methods in Geomechanics*, vol. 40, no. 12, pp. 1758–1770, 2016.

[139] J. Köbler, N. Magino, H. Andrä, F. Welschinger, R. Müller and M. Schneider, 'A computational multi-scale model for the stiffness degradation of short-fiber reinforced plastics subjected to fatigue loading,' *Computer Methods in Applied Mechanics and Engineering*, vol. 373, p. 113 522, 2021.

[140] N. Magino, J. Köbler, H. Andrä, F. Welschinger, R. Müller and M. Schneider, 'A space-time upscaling technique for modeling high-cycle fatigue-damage of short-fiber reinforced composites,' *Composites Science and Technology*, vol. 222, p. 109 340, 2022.

[141] A. P. Dey, F. Welschinger, M. Schneider, J. Köbler and T. Böhlke, 'On the effectiveness of deep material networks for the multi-scale virtual characterization of short fiber-reinforced thermoplastics under highly nonlinear load cases,' *Archive of Applied Mechanics*, vol. 94, no. 5, pp. 1177–1202, 2024.

[142] A. Paszke, 'Pytorch: An imperative style, high-performance deep learning library,' *arXiv:1912.01703*, 2019.

[143] M. Cranmer, 'Interpretable Machine Learning for Science with PySR and SymbolicRegression.jl,' *arXiv:2305.01582*, 2023.

[144] M. Safaei, M.-G. Lee and W. De Waele, 'Evaluation of stress integration algorithms for elastic–plastic constitutive models based on associated and non-associated flow rules,' *Computer Methods in Applied Mechanics and Engineering*, vol. 295, pp. 414–445, 2015.

[145] K. Runesson, S. Sture and K. Willam, 'Integration in computational plasticity,' *Computers & Structures*, vol. 30, no. 1, pp. 119–130, 1988.

[146] H. L. Schreyer, R. F. Kulak and J. M. Kramer, 'Accurate numerical solutions for elastic-plastic models,' *Journal of Pressure Vessel Technology*, vol. 101, no. 3, pp. 226–234, 1979.

[147] J. Ling, R. Jones and J. Templeton, 'Machine learning strategies for systems with invariance properties,' *Journal of Computational Physics*, vol. 318, pp. 22–35, 2016.